Relic Abundance of WIMPs in Non-standard Cosmological Scenarios

Dissertation

zur

Erlangung des Doktorgrades (Dr. rer. nat.)

der

Mathematisch-Naturwissenschaftlichen Fakultät

der

Rheinischen Friedrich-Wilhelms-Universität Bonn

vorgelegt von

Wuernisha Yimingniyazi
(Hoernisa Iminniyaz)

aus

Qitai, China

Bonn 2007

Angefertigt mit Genehmigung der Mathematisch-Naturwissenschaftlichen Fakultät der Rheinischen Friedrich-Wilhelms-Universität Bonn.

Diese Dissertation ist auf dem Hochschulschriftenserver der ULB Bonn
`http:\\hss.ulb.uni-bonn.de\diss_online` im Jahre 2007 elektronisch publiziert.

1. Referent: Prof. Dr. Manuel Drees
2. Referent: Prof. Dr. Herbert Dreiner
Tag der Promotion: 06.08.2007

Ich versichere, daß ich diese Arbeit selbständig verfaßt und keine anderen als die angegebenen Quellen und Hilfsmittel benutzt sowie die Zitate kenntlich gemacht habe.

Abstract

In this thesis we study the relic density n_χ of non–relativistic long–lived or stable particles χ in various non–standard cosmological scenarios. First, we discuss the relic density in the non–standard cosmological scenario in which the temperature is too low for the particles χ to achieve full chemical equilibrium. We also investigated the case where χ particles are non–thermally produced from the decay of heavier particles in addition to the usual thermal production. In low temperature scenario, we calculate the relic abundance starting from arbitrary initial temperatures T_0 of the radiation–dominated epoch and derive approximate solutions for the temperature dependence of the relic density which can accurately reproduces numerical results when full thermal equilibrium is not achieved. If full equilibrium is reached, our ansatz no longer reproduces the correct temperature dependence of the χ number density. However, we can contrive a semi–analytic formula which gives the correct final relic density, to an accuracy of about 3% or better, for all cross sections and initial temperatures. We also derive the lower bound on the initial temperature T_0, assuming that the relic particle accounts for the dark matter energy density in the universe. The observed cold dark matter abundance constrains the initial temperature $T_0 \geq m_\chi/23$, where m_χ is the mass of χ. Second, we discuss the χ density in the scenario where the Hubble parameter is modified. Even in this case, an approximate formula similar to the standard one is found to be capable of predicting the final relic abundance correctly. Choosing the χ annihilation cross section such that the observed cold dark matter abundance is reproduced in standard cosmology, we constrain possible modifications of the expansion rate at $T \sim m_\chi/20$, well before Big Bang Nucleosynthesis.

Contents

Chapter 1

Introduction

1.1 Motivation

Recent cosmological observations of cosmic microwave background (CMB) anisotropy by the Wilkinson Microwave Anisotropy Probe (WMAP) provide precise values for the cosmological parameters. In particular, the amount of cold Dark Matter (DM) density has been measured with good precision [1],

$$0.08 < \Omega_{\rm DM} h^2 < 0.12 \quad (95\% \text{ C.L.}) \,. \tag{1.1}$$

One of the mysterious questions as to cold DM is which kind of particle constitute cold dark matter. Since there exists no candidate particle for cold DM in the Standard Model (SM) of particle physics, we are obliged to consider physics beyond the SM looking for cold DM candidate particles [2, 3]. Moreover, this very restrictive range for the cold DM energy density requires particle physics models which posses dark matter candidates to provide the exactly same amount of cold DM as the observed value. In other words, this precise information allows us to test various models and constrain the parameter space of surviving models.

So far, many dark matter candidate particles have been proposed. Among them neutral, long–lived or stable weakly interacting massive particles (WIMPs) χ are excellent candidates. WIMPs are assumed to have the mass of around the weak scale, $m_\chi \sim 10 - 1000$ GeV. It is noticed that its characteristic pair annihilation cross section into lighter particles is $\sigma v \sim \pi\alpha^2/m_\chi^2$, where v is the relative velocity of the two annihilating WIMPs and α is a coupling constant of oder of the weak coupling constant. The standard scenario for dark matter production assumes that the temperature of the early universe was high enough

for completely thermalizing WIMPs and that WIMPs were decoupled from the thermal background when they were non–relativistic. Amazingly enough, based on the above assumptions the predicted relic abundance naturally results in the right order of magnitude for the DM abundance.

One of the best motivated candidates for WIMPs is the lightest neutralino in supersymmetric (SUSY) models. Assuming that the neutralino is the lightest supersymmetric particle (LSP) stabilized due to R–parity, its relic abundance has been extensively discussed [3–6]. Other WIMPs appear in models with universal extra dimensions (UED), where the cold DM candidate is the lightest first excited mode stabilized by KK–parity [7, 8]. In the minimal UED model, the partner of the hypercharge gauge boson is the lightest Kaluza–Klein particle (LKP). In little Higgs models with T–parity, scalars, the partner of hypercharge gauge boson and a heavy neutrino can be cold DM candidates [9–11]. In many cases the cosmologically favored parameter space of WIMP models can be directly tested at the CERN Large Hadron Collider (LHC) in a few years [12]. The same parameter space often also leads to rates of WIMP interactions with matter within the sensitivity of near–future direct DM detection experiments.

Except WIMPs, there are some other candidates in the extensions of the SM. For example, axions, which originally appeared to solve the strong CP problem in particle physics [13], are also dark matter candidates. Their mass is constrained by astrophysical and cosmological arguments to lie in the range $m \sim 10^{-5} - 10^{-2}$ eV [13]. Gravitinos, the supersymmetric partner of graviton and axinos, the fermionic partner of axion can also be DM candidates.

The consistency between the observed value of cold dark matter and the predicted value of relic density of thermal WIMPs lets us examine cosmological scenarios with experiments at high–energy colliders as well as DM searches. In this respect we should emphasize that the relic abundance of thermally produced WIMPs depends not only on their annihilation cross section, which can be determined by particle physics experiments, but also in general on the cosmological parameters during the era of WIMP production and annihilation. Of particular importance are the initial temperature T_0 at which WIMPs began to be thermally produced, and the expansion rate of the universe H.

Bearing this situation in mind, let us take a closer look at the standard cosmological scenario for WIMP production. It is assumed that the WIMPs were in full thermal and chemical equilibrium in the radiation–dominated epoch after the period of last entropy

production, which in standard cosmology means after the end of inflation. In this scenario the χ number density $n_\chi(T)$ drops exponentially once the temperature T falls below the mass m_χ of the relic particles, until the freeze–out temperature T_F is reached, at which point the interaction rate Γ is no longer larger than the expansion rate H of the universe and χ particles can not annihilate efficiently with each other and thus they decouple. The relic density remains almost constant from that time. In this case an accurate analytical expression for $n_\chi(T \ll T_F)$ have been derived [6, 14]; one finds that the χ relic density is essentially inversely proportional to the thermal average of the effective χ annihilation cross section into lighter particles and there is no dependence on the initial temperature T_0.

It should be noted that in non–standard scenarios the relic density can be larger or smaller than the value in the standard scenario. One example is the case where T_0 is smaller than or comparable to T_F, which can be realized in inflationary models with low reheat temperature. Since in many models the inflationary energy scale must be much higher than m_χ in order to correctly predict the density perturbations [15], the standard assumption $T_0 > T_F$ is not unreasonable. On the other hand, the constraint on the reheat temperature from Big Bang Nucleosynthesis (BBN) is as low as $T_0 \gtrsim$ MeV [16, 17]. From the purely phenomenological viewpoint, it is therefore also interesting to investigate the production of WIMPs in low reheat temperature scenarios [18–21].

We should emphasize at this point that the reheat temperature T_R may not be the highest temperature of the thermal plasma after inflation. If there is sufficiently fast thermalization, the inflaton decay products can attain a temperature $T_{\rm max} \gg T_R$ while the total energy density of the universe is still dominated by inflatons [2]. Therefore χ particles may have been in thermal equilibrium for some range of temperatures $T > T_R$ [16, 18, 22–24], even if they were never in equilibrium in the radiation–dominated epoch. However, an analytical treatment of the reheating epoch where $T > T_R$ was possible faces several complications not present in the radiation–dominated epoch: the entropy density was not constant, non–perturbative (and non–exponential) inflaton decays might have been important [25], and there might have been significant non–thermal sources of χ particles [23, 24, 26]. On the other hand, in supersymmetric scenarios thermalization of the inflaton decay products might be delayed by large vacuum expectation values of scalar fields along flat directions of the potential [27]. In our work we evade these complications by treating the χ number density at some initial temperature T_0 as a free parameter; in the absence of late entropy production, T_0 should be close to the reheat temperature T_R (depending on the exact definition of T_R).

The standard scenario also assumes that entropy per comoving volume is conserved for all temperatures $T \leq T_F$. Late entropy production can dilute the predicted relic density [28, 29]. The reason is that the usual calculation actually predicts the ratio of the WIMP number density to the entropy density. On the other hand, if late decays of a heavier particle non–thermally produce WIMPs in addition to the usual thermal production mechanism, the resulting increase of the WIMP density competes with the dilution caused by the decay of this particle into radiation, which increases the entropy density [20, 22–24, 30, 31].

Another example of a non–standard cosmology changing the WIMP relic density is a modified expansion rate of the universe. This might be induced by an anisotropic expansion [29], by a modification of general relativity [29, 32], by additional contributions to the total energy density from quintessence [33], by branes in a warped geometry [34], or by a superstring dilaton [35].

These examples show that, once the WIMP annihilation cross section is fixed, with the help of precise measurements of the cold dark matter density we can probe the very early stage of the universe at temperatures of $\mathcal{O}(m_\chi/20) \sim 10$ GeV. This is reminiscent of constraining the early evolution of the universe at $T = \mathcal{O}(100)$ keV using the primordial abundances of the light elements produced by BBN.

1.2 Purpose of the Thesis

The main purpose of this thesis is to investigate to what extent the constraint (1.1) on the WIMP relic abundance might allow us to derive quantitative constraints on modifications to the standard cosmological scenario for WIMP production [36]. So far the history of the universe has been established by cosmological observations as far back as the BBN era. In this thesis we try to derive bounds on cosmological parameters relevant to the era before BBN. Rather than studying specific extensions of the standard cosmological scenario, we simply parameterize deviations from the standard scenario, and attempt to derive constraints on these new parameters. Since we only have the single constraint (1.1), for the most part we only allow a single quantity to differ from its standard value. We expect that varying two quantities simultaneously will allow to get the right relic density for almost any WIMP annihilation cross section. This has been shown explicitly in [20] for the case that both late entropy production and non–thermal WIMP production are

considered, even if both originate from the late decay of a single scalar field.

The first part of our work is devoted to the discussion of relic abundance of non–relativistic, long–lived or stable particles χ in low temperature scenarios. We assume particles never reach thermal equilibrium in the radiation–dominated era because of the low reheat temperature after inflation. If χ annihilation can be neglected, one finds that the contribution to the χ relic density from thermal production is directly proportional to the cross section. We developed an approximate analytic treatment that also works in the intermediate region, where (for some range of temperatures) both thermal production and annihilation of χ particles were important. It is based on an expansion in the effective annihilation cross section. To leading order, only the production term is kept in the Boltzmann equation describing the evolution of number density of χ particles; this corresponds to the "completely out of equilibrium" scenario. We add the correction to the leading order solution due to the χ annihilation effect and treat it as a small perturbation. The first oder result is linear to the annihilation cross section σ, while the correction is $\mathcal{O}(\sigma^3)$ if we start from vanishing initial abundance. The surprising result is that the terms of higher order in cross section can be "re–summed" using a simple trick. This can be shown to be exact in the simple case where the initial abundance is nonzero and thermal production of χ particles is negligible and works numerically also for non–negligible thermal production.

The above–mentioned study is useful when we analyze the dependence of the WIMP abundance on the initial temperature T_0 of the conventional radiation–dominated epoch. We show that for fixed T_0 the predicted WIMP relic density reaches a maximum as the annihilation cross section is varied from very small to very large values. A small annihilation cross section corresponds to a large $T_F > T_0$; in this case the relic density increases with the annihilation cross section, since WIMP production from the thermal plasma is more important than WIMP annihilation. On the other hand, increasing this cross section reduces T_F; once $T_F < T_0$ a further increase of the cross section leads to smaller relic densities since in this case WIMPs continue to annihilate even after the temperature is too low to produce WIMP production. Here we turn this argument around, and derive the lower bound on $T_0 \geq m_\chi/23$ under the assumption that all WIMPs are produced thermally. Notice that we do not need to know the WIMP annihilation cross section to derive this bound.

In the second part of our work, we discussed the non–standard cosmological scenario for modified expansion rate. We examine the dependence of the WIMP relic abundance on the expansion rate in an epoch prior to BBN, with the expansion parameter allowed to depart

from the standard value. We find that the standard method of calculating the thermal relic density [2, 14] is found to be still applicable to the scenario with modified expansion rate. Here in order to avoid unnecessarily complicated calculation we employ a generic Taylor expanded form for the temperature dependence of the modification factor of the expansion rate, which should eventually fall into around unity before BBN starts. The change of the Hubble parameter results in different relic abundances.

1.3 Organization of the Thesis

This thesis is organized as follows: in Chapter 2, we briefly mention the evidences for dark matter existence, candidate particles for dark matter and the experimental detection for dark matter. In Chapter 3, we review the calculation of relic abundance in the standard cosmological scenario, where it is assumed that the relic particles attained full thermal equilibrium. In Chapter 4, we discuss the calculation of the χ relic abundance in scenarios where the temperature was too low for χ particles to have been in full equilibrium. Here we also derive the lower bound on the initial temperature T_0. In Chapter 5, the relic abundance including the decay of heavier particles to χ is investigated. In Chapter 6, we study the relic abundance in the scenario where the pre–BBN expansion rate is allowed to depart from the standard one. Using approximate analytic formulae for the predicted WIMP relic density for this modified expansion rate scenario, we derive constraints on the early expansion parameter. The last chapter is devoted to conclusions and discussion.

Chapter 2

Dark Matter Puzzle

Dark matter is the matter which does not emit or reflect a detectable amount of electromagnetic radiation at any wavelength. However, its presence can be inferred from its gravitational interactions on the visible matter. Although the evidence for dark matter was noticed by Swiss astronomer F. Zwicky in 1933 through studying the motion of galaxies in Coma cluster [37], its existence is practically accepted in recent years due to the wide range of observational evidences like CMB anisotropy [1], galaxy surveys [38, 39], etc. Despite of such compelling evidences for the existence of dark matter, the composition of dark matter is still unclear. This situation makes dark matter as one of the hottest research topic in particle physics, cosmology and astronomy. From particle physics point of view, many candidates for dark matter have been proposed. Now many experiments are ongoing and planned aiming for detecting non–baryonic cold dark matter particles. This chapter is devoted to review of the evidences for the existence of non–baryonic cold dark matter in various cosmological scales, the proposed candidates for dark matter and the dark matter detection experiments.

2.1 Evidences for Dark Matter

The most reliable evidence for dark matter on galactic scale comes from the analysis of the rotation curves of spiral galaxies. The galaxy rotation curves show the circular velocities of stars and gas clouds as function of the distance r from the galactic center. If the galaxy has mass $M(r)$ in radius r, then the balance between the centrifugal acceleration and the gravitational pull demands that its velocity obeys

$$\frac{v^2}{r} = \frac{G_N M(r)}{r^2}, \tag{2.1}$$

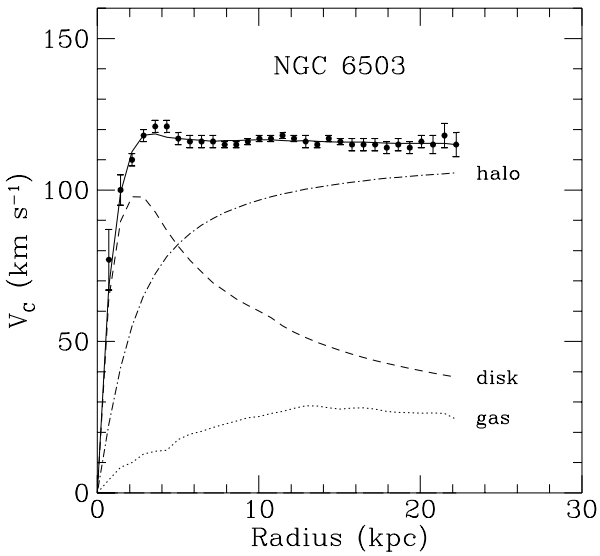

Figure 2.1: Rotation curve of NGC 6503. The dotted, dashed and dash-dotted lines are the contributions of gas, disk and dark matter, respectively [40].

where $G_N = 6.67 \times 10^{-8}$ cm^3 g^{-1} sec^{-2} is Newton's gravitational constant. The above equation can be rewritten as

$$v = \sqrt{\frac{G_N M(r)}{r}}. \tag{2.2}$$

According to Newtonian gravity theorem, the mass outside the radius has no contribution to the gravitational pull at all. If the mass is only in its visible part, the velocity should drop at large radii as $v \propto 1/\sqrt{r}$. Instead, at such large distance, observed rotation curves show the velocity remains almost constant as shown in Fig. 2.1 [40]. The fact that $v(r)$ is approximately constant implies the existence of dark halo with $M(r) \propto r$ or $\rho \propto 1/r^2$. The abundance of a substance i in the universe (matter, radiation or vacuum energy) is expressed in units of the critical density $\rho_{\rm crit}$ as $\Omega_i \equiv \rho_i/\rho_{\rm crit}$, where the critical density is defined by $\rho_{\rm crit} = 3H_0^2 M_{\rm Pl}^2 = 1.05 \times 10^{-5}\ h^2$ GeV cm^{-3} with H_0 being the Hubble constant and $M_{\rm Pl} = 1/\sqrt{8\pi G_N} = 2.4 \times 10^{18}$ GeV the reduced Planck mass, where $h \simeq 0.7$ is the scaled Hubble constant in units of 100 km Mpc^{-1} sec^{-1}. The mass density averaged over the entire universe is then $\Omega = \sum_i \Omega_i = \sum_i \rho_i/\rho_{\rm crit}$. When the total energy density is equal to the critical density, $\Omega = 1$, the universe is flat. Galactic rotation curves imply $\Omega_M \gtrsim 0.1$.

Additional evidence for dark matter at galactic scales comes from mass modeling of the detailed rotation curves, including spiral arm features [41]. Some elliptical galaxies show

evidence for dark matter via strong gravitational lensing [42].

The evidence from the cluster scale actually was noticed by F. Zwicky in 1933 as we mentioned earlier, he inferred [37], from measurements of the velocity dispersion of galaxies in the Coma cluster, a mass–to–light ratio of around 400 solar masses per solar luminosity, thus exceeding the ratio in the solar neighborhood by two orders of magnitude. Today, most dynamical estimates [43–45] are consistent with a value $\Omega_M \sim 0.2 - 0.3$ on cluster scales.

The observation of the large scale structure bounds the relic density of the matter component. Sloan Digital Sky Survey (SDSS) reported $\Omega_M h^2 = 0.130 \pm 0.010$ for $\Omega_b h^2 = 0.024$ [46]. The value for the matter density obtained from the large scale structure is more precise than the values from the galaxy scale and cluster scale.

Today, the WMAP precision data enable us to accurately test cosmological models and put stringent constraints on cosmological parameters [1]. The WMAP data are powerful because they result from a mission that was carefully designed to limit systematic errors [47, 48]. From the analysis of WMAP data alone, the abundances of baryons and matter in the universe are found to be

$$\Omega_b h^2 = 0.0223^{+0.0007}_{-0.0009}, \qquad \Omega_M h^2 = 0.127^{+0.007}_{-0.010}. \tag{2.3}$$

Figure 2.2 shows the energy contents of the universe for the flat ΛCDM model [51].

The matter density obtained from WMAP data is consistent with the matter density from large scale structure. On the other hand, BBN provides us a stringent constraint on the baryon abundance. The value of $\Omega_b h^2$ obtained from WMAP data is also consistent with the predictions from BBN [49, 50],

$$0.017 < \Omega_b h^2 < 0.024 \ \ (95\% \text{ C.L.}) \,. \tag{2.4}$$

The difference between $\Omega_M h^2$ and $\Omega_b h^2$ shows the dark matter should be non–baryonic. What kind of particle can be a dark matter particle? Up to now, there are many candidates proposed in particle physics. In the next, we review the candidates for dark matter.

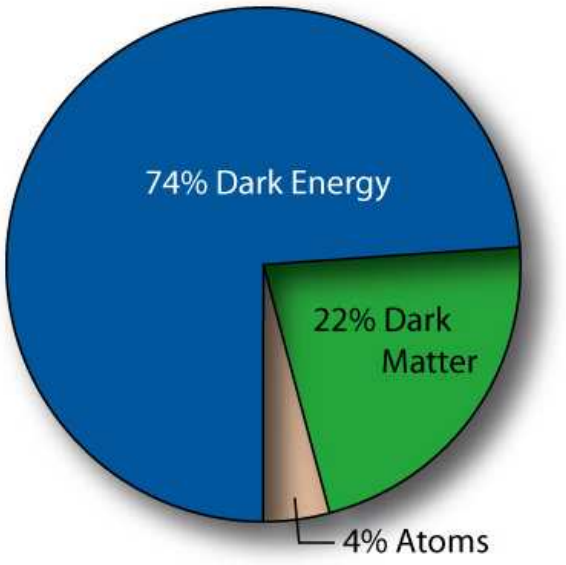

Figure 2.2: Energy contents of the universe reported by WMAP [51].

2.2 Candidate Particles for Dark Matter

It was shown that baryons can not reach the required amount of dark matter by the results reported by the observations of CMB, the primordial light element abundances, the large scale structure of the universe as mentioned in the previous section. Before going to the discussion of viable candidates, we mention some excluded candidates.

Massive Compact Halo Objects (MACHOs) [52] are astronomical objects which are too dark to be detected and thus can be conservative candidates in the sense that no unknown particle physics model is required. Some part of the baryonic component of the energy density may contribute to MACHOs, for example, brown dwarfs, Jupitars, neutron stars and white dwarfs. Using the gravitational microlensing effect, MACHOs in the mass range of $0.6 \times 10^{-7} M_{\odot} < M < 15 M_{\odot}$ are ruled out as the primary constituent of our galactic halo. This result supports the need for non–baryonic DM.

Neutrinos are the only existing hot dark matter candidate particles in the SM [53]. If the neutrinos were in full equilibrium, their total relic density is predicted to be

$$\Omega_{\nu} h^2 = \sum_{i=1}^{3} \frac{m_{\nu_i}}{94 \text{ eV}}, \tag{2.5}$$

where m_{ν_i} is the mass of i–th neutrino. From the tritium β–decay experiments [54], an upper limit on the electron–type neutrino mass is obtained as $m_{\nu_e} < 2.0$ eV. Since the mass differences among the three mass eigenvalues must be very small to explain the solar $\Delta m^2_{\odot} = 8 \times 10^{-5}$ eV^2 and atmospheric $\Delta m^2_{\oplus} = 2.5 \times 10^{-3}$ eV^2 neutrino anomalies [55], electron–volt scale neutrinos should be nearly degenerate. Then the maximum contribution to the matter density is $\Omega_\nu h^2 < 0.064$. Moreover, combination of the WMAP, galaxy clustering and supernovae data put the constraint on the neutrino relic density $\Omega_\nu h^2 < 0.0072$ (95% C.L.) [1]. This implies a limit on neutrino mass, $\sum_i m_{\nu_i} < 0.68$ eV, assuming the usual number density of fermions which decoupled when they were relativistic. From the above discussions we conclude the neutrinos are not abundant enough to be the dominant component of dark matter. Therefore, we have to go beyond the SM to search for dark matter candidates.

WIMPs are most favorable and widely studied cold dark matter candidates in particle physics. They appear in the extension of the SM. WIMPs as DM candidate should be electrically neutral and long lived or stable particles. The mass scale of WIMPs is in the range of the electroweak scale. They interact with ordinary matter only through the weak force and gravity. Since these particles have roughly the same coupling strength as leptons, it is expected that a large amount of WIMPs were produced in the early universe. As the universe cools down, the interaction rate of WIMPs becomes weaker and they finally decouple from the thermal bath. Their relic density remains almost constant after the decoupling and found to be naturally consistent with the observed dark matter abundance. This agreement between observation and theory makes WIMPs very attractive dark matter candidates.

The best motivated WIMP is the lightest supersymmetric particle, plausibly neutralino [3]. In Minimal Supersymmetric Standard Model (MSSM), the lightest neutralino is a mixture of the superpartner of B boson (bino), W^0 boson (wino), and two neutral Higgs bosons (higgsino) present [56]. There is a quantum number called R–parity in supersymmetric models, which is defined as $R = (-1)^{3B+L+2S}$ with S being the spin, B the Baryon number and L the lepton number. All the SM particles are assigned R–parity of $R = +1$ while all the superpartners R–parity of $R = -1$. If R–parity is conserved, sparticles can only decay into an odd number of sparticles (plus SM particles). The lightest supersymmetric particle is, therefore, stable and can only be destroyed via pair annihilation. The relic density of neutralino are widely studied [3–6]. The LKP in UED models is also a good dark matter candidate. Typically the first KK excitation of the $U(1)_Y$ gauge boson is the LKP [8].

Let us turn to non–WIMP candidates. While axions are introduced in an attempt to solve strong CP problem in particle physics [13], axions are also considered as a dark matter candidate. Laboratory searches, stellar cooling and the dynamics of supernova 1987A constrain axions to be very light ($\lesssim 0.01$ eV). Furthermore, they are extremely weakly interacting with ordinary particles, which implies that they were not in thermal equilibrium in the early universe. The calculation of the axion relic density is uncertain, and depends on the assumptions made regarding the production mechanism. Nevertheless, it is possible to find an acceptable range where axions satisfy all the present–day constraints and saturate the dark matter density [13].

In addition to neutralinos, gravitinos and axinos are also considered as viable dark matter candidates in SUSY model. Gravitinos are the superpartners of graviton. In some supersymmetric scenarios, for example, the gauge mediated supersymmetry breaking scenario, gravitinos can be the lightest supersymmetric particles and be stable. Gravitinos are thus very strongly theoretically motivated dark matter candidates as well as neutralinos. With only gravitational interactions, however, gravitons are very difficult to observe [57]. Axinos, the superpartner of the axion, share similar phenomenological properties to gravitinos [58, 59].

Sterile neutrinos were proposed as dark matter candidates in 1993 by Dodelson and Widrow [60]. These hypothetical particles are similar to the SM neutrinos, but without SM weak interactions, apart from mixing. A Majorana mass of $\mathcal{O}$(KeV) for the sterile neutrino leads to warm dark matter. Sterile neutrinos can also be cold dark matter, if there is very small lepton asymmetry, in which case they are produced resonantly with a non–thermal spectrum [61].

2.3 Dark Matter Detection

Because WIMPs only interact with matter via the gravitational and weak forces, they are difficult to detect. However, experimental searches for these dark matter candidates are conducting and ongoing. The searches for these particles are divided into two categories, one is direct detection, in which the dark matter particles are observed in a detector. If the galaxy is filled with WIMPs, then hundreds of thousands of WIMPs should pass through the Earth, and making it possible to look for the interaction of such particles with matter,

e.g. by recording the recoil energy of nuclei, as WIMPs scatter of them [62–65]. Many direct detection experiments are either now operating or are currently in development. Some of these direct experiments have already produced quite strong limits on the elastic scattering cross section with protons or neutrons of potential dark matter candidates. DAMA experiment reported an annual modulation of their event rate consistent with the detection of a WIMP with a mass of approximately 60 GeV and a scattering cross section of the order of 10^{-41} cm^2 [66]. However, the result from DAMA experiment is conflict with other experiments, such as EDELWEISS [67] and CDMS [68]. They have explored the parameter space favored by DAMA without finding any evidence of dark matter. It is premature to think we have found experimental evidence for WIMPs. In the coming years, the experiments will improve on current limits by several orders of magnitude. In near future, hopefully we can detect WIMPs.

The second method is indirect detection, which looks for the products of annihilations of dark matter particles, either in the galactic halo or in Earth and Sun where WIMPs may have been accumulated by gravitational capture. If the dark matter annihilation takes place in galactic halo, these annihilation products may include gamma–rays, neutrinos, positrons and anti-protons.

There are observations for gamma–rays directly both from ground–based telescopes and space based telescopes. When photons interact in the atmosphere, they produce an electromagnetic cascade and thus a shower of secondary particles, allowing ground–based telescopes to indirectly observe gamma–rays through the detection of secondary particles and the Cerenkov light originating from their passage through the Earth's atmosphere. The first observation of Cerenkov light due to gamma–ray emission from an astrophysical source was the detection of the Crab Nebula with Whipple observatory 10m reflector [69]. Currently, only six TeV gamma–ray sources have been confirmed, above 10 GeV, having been detected by multiple experiments at a high significance level and they have not been confirmed yet. Many experiments such as MAGIC [70], HESS [71] probably could detect more gamma–ray sources. The first high–energy GeV gamma–ray space telescope was EGRET (the Energetic Gamma–Ray Experiment Telescope), onboard the Compton gamma–ray observatory. EGRET was launched in 1991, it has observed the universe in a range of energies extending up to approximately 30 GeV, amassing a large catalog of observed gamma–ray sources, although around 60% of these sources remain unidentified [72]. The EGRET experiment has reported an excess for gamma–rays in the region of the galactic center, in an error circle of 0.2 degree radius including the positron l=0(deg) and b=0(deg) [73]. The EGRET

source is not exactly coincident with the galactic center [72]. This makes the interpretation of the EGRET signal as dark matter annihilation in a density spike problematic. The next space–based gamma–ray observatory will be GLAST (Gamma–ray Large Area Space Telescope), which is scheduled for lunch in 2007. GLAST will be sensitive to gamma–rays up to several hundred GeV in energy [3].

Neutrinos can be produced in the annihilations of dark matter particles in addition to gamma–rays. AMANDA, ANTARES, and IceCube are high–energy neutrino telescopes which aim to detect neutrinos from the annihilations of WIMPs. In the GeV–TeV energy range, neutrinos are most easily observed by their "muon" tracks produced in charged current interactions inside of or nearby the detector volume. These muons travel through the detector emitting Cerenkov light which allows their trajectory to be reconstructed. Though the experiments such as the Lake Baikal experiment [74] and AMANDA [75, 76] at the South Pole have observed neutrinos produced in the Earth's atmosphere, they have not, thus far, identified any extra–terrestrial neutrinos. The constructing experiments ANTARES [77] and IceCube [78, 79] will be more sensitive to neutrinos, we hope we can detect neutrinos from annihilation of WIMPs in these experiments.

The observation of cosmic positrons or anti–protons are also providing the evidence of dark matter annihilations. The HEAT (High–Energy Antimatter Telescope) experiments measured the spectrum of positrons between 1 and 30 GeV [80]. The results were very interesting, as they indicated an excess in the positron flux. This excess could be a signature of dark matter annihilation in the local galactic halo [3]. A second HEAT flight in 2000 confirmed this observation [81, 82].

The BESS (Balloon borne Experiment Superconducting Solenoidal spectrometer) experiment had provided the most detailed measurements of the cosmic anti–proton spectrum to date in the range of about 200 MeV to 3 GeV [83, 84]. Above this energy, up to about 40 GeV, the CAPRICE experiment provides the best anti–proton measurements [85]. There appears to be a mild excess in the anti–proton spectrum in the hundreds of MeV range, although it is very difficult to assess this result with any certainty. The ongoing or future experiments are likely more sensitive to the cosmic positrons and anti–proton spectra. The satellite borne PAMELA experiments measure the spectra of both cosmic positrons and anti–protons with considerably improved precision. The primary objective of PAMELA is to the measure the cosmic anti–proton spectrum in the range of 80 GeV to 190 GeV and the cosmic positron spectrum in the range of 50 MeV to 270 GeV, far beyond the energies

measured by HEAT, BESS or CAPRICE [86]. PAMELA is expected to measure these spectra to far greater precision than the previous experiments, especially at high energies (above $\sim$ 10 GeV).

Chapter 3

Relic Abundance in the Standard Cosmological Scenario

Although WIMPs are invented in the process of the attempt to solve puzzles in the context of particle physics, they have the relic abundance in the right regime to explain the dark matter in the universe by coincidence. In the standard cosmological scenario, it is assumed that WIMPs were in thermal equilibrium in the early universe and in abundance when the temperature was higher than the mass of the particles. The equilibrium abundance is maintained by the annihilation of WIMPs into lighter particles and by other particles annihilating into WIMPs. Following the cooling of the universe, the temperature falls below the WIMP mass and the equilibrium abundance drops exponentially until the annihilation rate Γ becomes smaller than the expansion rate H. At this point, the abundance of cosmological relics freezes out and remains almost constant until today. In this chapter we review the calculation of the relic density of WIMPs in the standard cosmological scenario.

3.1 Boltzmann Equation

We start the discussion of the relic density n_χ of stable or long–lived χ particles, by reviewing the structure of the Boltzmann equation which describes annihilation and creation of χ particles. Here we assume that χ particles are thermally produced and χ is self–conjugate[1], $\chi = \bar{\chi}$, and that some symmetry, for example R–parity, forbids decays of χ into SM particles; the same symmetry then also forbids single production of χ from the thermal background. However, the creation and annihilation of χ pairs remains allowed. The time evolution of the number density n_χ in the expanding universe is then described

[1]The case $\chi \neq \bar{\chi}$ differs in a non–trivial way only in the presence of a $\chi - \bar{\chi}$ asymmetry, i.e. if $n_\chi \neq n_{\bar{\chi}}$.

by the Boltzmann equation [2],

$$\frac{dn_\chi}{dt} + 3Hn_\chi = -\langle\sigma v\rangle(n_\chi^2 - n_{\chi,\mathrm{eq}}^2), \tag{3.1}$$

with $n_{\chi,\mathrm{eq}}$ being the equilibrium number density of the relic particles. The second term on the left hand side (LHS) of the equation describes the effect of the expansion of the universe. The prefactor in the RHS of Eq.(3.1) is the thermal average of the annihilation cross section σ multiplied with the relative velocity v of the two annihilating χ particles. The first (second) term on the right–hand side (RHS) of Eq.(3.1) describes the decrease (increase) of the number density due to annihilation into (production from) lighter particles. The Boltzmann equation assumes that χ is in kinetic equilibrium with the standard model particles.

The equilibrium number density in the Boltzmann equation (3.1) is given by

$$n_{\chi,\mathrm{eq}}(T) = g_\chi \int \frac{\mathrm{d}^3p}{(2\pi)^3} f_{\chi,\mathrm{eq}}(p,T), \tag{3.2}$$

where g_χ denotes the number of intrinsic degrees of freedom for χ particle (e.g. due to the spin and color). At low temperatures $T \ll m_\chi$, $f_{\chi,\mathrm{eq}}$ is the equilibrium distribution function which in the Maxwell–Boltzmann approximation is given by

$$f_{\chi,\mathrm{eq}} = \mathrm{e}^{-E/T}. \tag{3.3}$$

Therefore, the equilibrium number density is

$$n_{\chi,\mathrm{eq}} = g_\chi \left(\frac{m_\chi T}{2\pi}\right)^{3/2} \mathrm{e}^{-m_\chi/T}. \tag{3.4}$$

At high temperatures, χ are abundant and rapidly annihilate with its own antiparticle χ into the standard model particles f, $\bar{f}$ ($\chi\chi \propto f\bar{f}$) and vice versa. Shortly after T drops below m_χ ($T \ll m_\chi$), the number density of χ drops exponentially, until the annihilation rate $\Gamma_\chi = n_\chi\langle\sigma v\rangle$ becomes less than the expansion rate H. The temperature at which the particle decouples from the thermal bath is called freeze–out temperature T_F. Therefore χ particles are no longer able to annihilate efficiently and the number density per co–moving volume becomes almost constant.

It is useful to rewrite Eq.(3.1) in terms of the scaled inverse temperature $x = m_\chi/T$ as well as the dimensionless quantities $Y_\chi = n_\chi/s$ and $Y_{\chi,\mathrm{eq}} = n_{\chi,\mathrm{eq}}/s$. The entropy density

is given by $s = (2\pi^2/45) g_{*s} T^3$, where the effective number of the degrees of freedom g_{*s} is given by summing over all relativistic particle species in existence:

$$g_{*s} = \sum_{i=\text{bosons}} g_i \left(\frac{T_i}{T}\right)^3 + \frac{7}{8} \sum_{i=\text{fermions}} g_i \left(\frac{T_i}{T}\right)^3 , \tag{3.5}$$

with T_i being the temperature of species i. Assuming that the universe expands adiabatically, the entropy per comoving volume, sR^3, remains constant, which implies

$$\frac{ds}{dt} + 3Hs = 0 \,. \tag{3.6}$$

The time dependence of the temperature is then given by

$$\frac{dx}{dt} = \frac{Hx}{1 - \dfrac{x}{3g_{*s}} \dfrac{dg_{*s}}{dx}} . \tag{3.7}$$

Therefore the Boltzmann equation (3.1) can be written as

$$\frac{dY_\chi}{dx} = -\frac{\langle \sigma v \rangle s}{Hx} \left(1 - \frac{x}{3g_{*s}} \frac{dg_{*s}}{dx}\right) \left(Y_\chi^2 - Y_{\chi,\text{eq}}^2\right) . \tag{3.8}$$

Thermal production of WIMPs takes place during the radiation–dominated epoch. In this period, the expansion rate is given by

$$H = \frac{\pi T^2}{M_{\text{Pl}}} \sqrt{\frac{g_*}{90}}, \tag{3.9}$$

where

$$g_* = \sum_{i=\text{bosons}} g_i \left(\frac{T_i}{T}\right)^4 + \frac{7}{8} \sum_{i=\text{fermions}} g_i \left(\frac{T_i}{T}\right)^4 . \tag{3.10}$$

For $T \ll m_\chi$ the annihilation cross section can often (but not always) be approximated by the non–relativistic expansion in terms of v^2 [6], and its thermal average is

$$\langle \sigma v \rangle = a + b \langle v^2 \rangle + \mathcal{O}(\langle v^4 \rangle) = a + 6b/x + \mathcal{O}(1/x^2) \,. \tag{3.11}$$

Here a is the $v \to 0$ limit of the contribution to σv where the two annihilating χ particles are in an S wave. If S wave annihilation is suppressed, b describes the P wave contribution to σv. In principle, the parameters a and b are calculable once we specify the model. In the rest of the thesis we adopt a model–independent approach and treat a and b as free parameters.

3.2 Approximate Solution for the Boltzmann Equation

The Boltzmann equation (3.8) can be solved numerically while no general analytical solution to Eq.(3.8) exists. One can solve this differential equation approximately to a very good accuracy [2, 6]. In terms of the variable $\Delta = Y_\chi - Y_{\chi,\mathrm{eq}}$, the Boltzmann equation can be rewritten as

$$\frac{d\Delta}{dx} \simeq -\frac{dY_{\chi,\mathrm{eq}}}{dx} - \frac{4\pi}{\sqrt{90}} m_\chi M_{\mathrm{Pl}} \frac{G(x)\langle\sigma v\rangle}{x^2} \Delta(2Y_{\chi,\mathrm{eq}} + \Delta), \tag{3.12}$$

where

$$G(x) = \frac{g_{*s}}{\sqrt{g_*}} \left(1 - \frac{x}{3g_{*s}} \frac{dg_{*s}}{dx}\right). \tag{3.13}$$

The solution can be discussed in two extreme regimes. At early times ($x \ll x_F$), Y_χ tracks its equilibrium value $Y_{\chi,\mathrm{eq}}$ very closely. Therefore Δ and $d\Delta/dx$ are small. Ignoring Δ^2 and $d\Delta/dx$, we obtain

$$\Delta = \frac{x^2}{(8\pi/\sqrt{90}) m_\chi M_{\mathrm{Pl}} G(x) \langle\sigma v\rangle}, \tag{3.14}$$

where we used $dY_{\chi,\mathrm{eq}}/dx \simeq -Y_{\chi,\mathrm{eq}}$ for $x \gg 1$. At late times ($x \gg x_F$), one can ignore the production term in the Boltzmann equation:

$$\frac{d\Delta}{dx} = -\frac{4\pi}{\sqrt{90}} m_\chi M_{\mathrm{Pl}} \frac{G(x)\langle\sigma v\rangle}{x^2} \Delta^2. \tag{3.15}$$

Integrating this equation from x_F to infinity and assuming $\Delta(x_F) \gg \Delta(\infty)$, we have

$$Y_{\chi,\infty} \equiv Y_\chi(x \gg x_F) = \frac{x_F}{1.32 m_\chi M_{\mathrm{Pl}} \sqrt{g_*(x_F)} (a + 3b/x_F)}, \tag{3.16}$$

where we used the non–relativistic expansion of $\langle\sigma v\rangle$ and assumed $g_* \simeq g_{*s}$, $dg_{*s}/dx \simeq 0$. As we mentioned in Chapter 2, conventionally the energy density of χ is expressed as $\Omega_\chi = \rho_\chi/\rho_{\mathrm{crit}}$. The present energy density of the relic particle is given by $\rho_\chi = m_\chi n_{\chi,\infty} = m_\chi s_0 Y_{\chi,\infty}$, with $s_0 \simeq 2900\ \mathrm{cm}^{-3}$ being the present entropy density. Therefore, we obtain the standard approximate formula for the relic density:

$$\begin{aligned} \Omega_\chi h^2 &= \frac{\rho_\chi}{\rho_{\mathrm{crit}}} h^2 = \frac{m_\chi s_0 Y_{\chi,\infty}}{3M_{\mathrm{Pl}}^2\ (100\ \mathrm{km\ sec^{-1}\ Mpc^{-1}})^2} \\ &= 2.7 \times 10^{10}\ Y_{\chi,\infty} \left(\frac{m}{100\ \mathrm{GeV}}\right). \end{aligned} \tag{3.17}$$

Using Eq.(3.16), we obtain

$$\Omega_\chi h^2 \simeq \frac{8.5\times10^{-11}\ x_F\ \mathrm{GeV}^{-2}}{\sqrt{g_*(x_F)}(a+3b/x_F)} \simeq 0.2\left(\frac{a+3b/x_F}{1\times10^{-9}\ \mathrm{GeV}^{-2}}\right)^{-1}\left(\frac{x_F}{22}\right)\left(\frac{g_*(x_F)}{90}\right)^{-1/2}. \quad (3.18)$$

Note that the relic density of the particle is inversely proportional to the annihilation cross section and that there is no explicit dependence on the mass of the particle. Calculating the cross section and the freeze–out temperature is sufficient for predicting the relic density. Freeze–out occurs when the deviation Δ is of the same order as the equilibrium value:

$$\Delta(x_F) = \xi Y_{\chi,\mathrm{eq}}(x_F), \quad (3.19)$$

where ξ is a numerical constant of oder unity. Substituting the early time solution of Eq.(3.14) into this equation, x_F is obtained by iteratively solving

$$x_F = \ln\frac{0.382\ \xi m_\chi M_{\mathrm{Pl}} g_\chi (a+6b/x_F)}{\sqrt{x_F g_*(x_F)}}. \quad (3.20)$$

It is known that if we choose $\xi = \sqrt{2}-1$, the standard formula (3.18) gives a good approximation of exact numerical results for the relic density. The decoupling temperature depends only logarithmically on the cross section, typically $x_F \simeq 22$. Figure. 3.1 shows the numerical solution to the Boltzmann equation (3.8). Here we take $m = 100$ GeV, $g_\chi = 2$, $g_* = 90$ (constant), $a = 1\times10^{-8}$ GeV^{-2}. The figure clearly shows that the freeze–out occurred around $x_F = 22$ and after the decoupling point the relic abundance of χ particles shows almost constant as mentioned earlier. Since the typical mass scale of WIMPs is around weak scale, $m_\chi \sim 100$ GeV, the annihilation cross section is typically given by $\langle\sigma v\rangle = \pi\alpha^2/m_\chi \sim 10^{-9}$ GeV^{-2}, from (3.18) we find that the predicted WIMP relic density $\Omega_\chi h^2$ can naturally be consistent with the observed cold DM energy density $\Omega_{\mathrm{DM}}h^2$.

The approximate solution (3.18) of Boltzmann equation (3.8) is not always applicable. There are three exceptions where the standard methods of calculating relic abundance which we reviewed above fails [6]. For example, when the relic particles are the lightest of a set of similar particles whose masses are nearly degenerate, the relic abundance of the lightest particle is determined not only by its annihilation cross section, but also by the annihilation of the heavier particles, which will decay into the lightest. This process is called "coannihilation". An example of the coannihilation is a light squark with neutralino dark matter. The second situation occurs when the relic particles lies near a mass threshold. The annihilation into particles heavier than the relic particles was considered kinematically

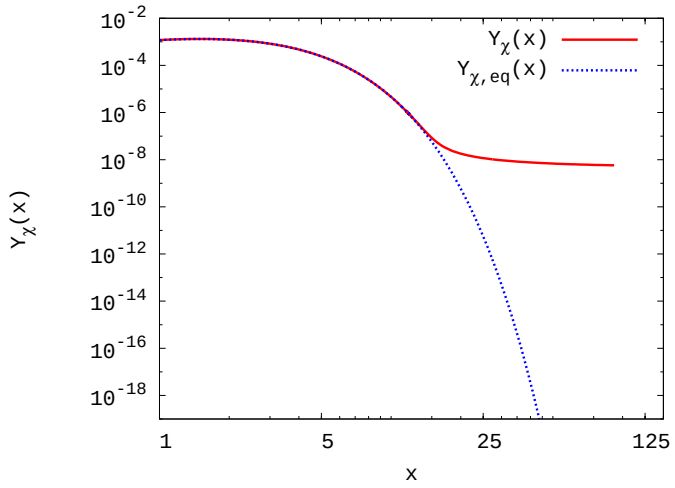

Figure 3.1: Evolution of $Y_\chi(x)$ (solid red) and $Y_{\chi,\mathrm{eq}}$ (blue dotted) as function of x for $m = 100$ GeV, $g_\chi = 2$, $g_* = 90$ (constant), $a = 1 \times 10^{-8}$ GeV^{-2}, $b = 0$.

forbidden, however, if the mass difference is $\sim 5 - 15\%$, these "forbidden" channels can dominate the cross section and determine the relic abundance. The third case where the standard method fails is the case when the annihilation takes place near a pole in the cross section. In this thesis, in order to extract the effect caused by the low maximal temperature and the modification of the Hubble parameter clearly, we discard the three exceptional cases. In the following chapters, we will discuss the relic density of χ particles in non–standard cosmological scenario.

Chapter 4

Relic Abundance in a Low–Temperature Scenario

In the previous chapter we calculate the relic density according to the assumption that the particles were in thermal equilibrium in the early universe and decoupled when they were non–relativistic. If we look at the final result (3.18), the relic density is anti–proportional to the annihilation cross section. This result leads to high relic density unless the cross section is as large as $\sim 10^{-9}$ GeV^{-2}. Bearing this situation in mind, it is important to explore scenarios where the relic density comes out smaller than the standard calculation and find a useful formula which properly describes the behavior of the relic abundance. On the other hand, We have direct evidence from BBN for temperatures below MeV ($T <$ (few) MeV) [16,17]. From a phenomenological view point, we assume particles never reach thermal equilibrium because of the low reheat temperature after inflation. We start from some initial temperature with vanishing or non–vanishing initial abundance. We solve the Boltzmann equation based on this assumption and try to find suitable analytic formula for the relic density in low temperature scenario.

4.1 Numerical Results

In this section, we solve the Boltzmann equation (3.8) numerically. For later convenience we first rewrite the Boltzmann equation (3.8), using Eqs.(3.4) and (3.11):

$$\frac{dY_\chi}{dx} = -f\left(a + \frac{6b}{x}\right)\frac{1}{x^2}\left(Y_\chi^2 - cx^3\mathrm{e}^{-2x}\right) , \tag{4.1}$$

where

$$f = 1.32\sqrt{g_*}m_\chi M_{\rm Pl} , \quad c = 0.0210\, g_\chi^2/g_*^2 \tag{4.2}$$

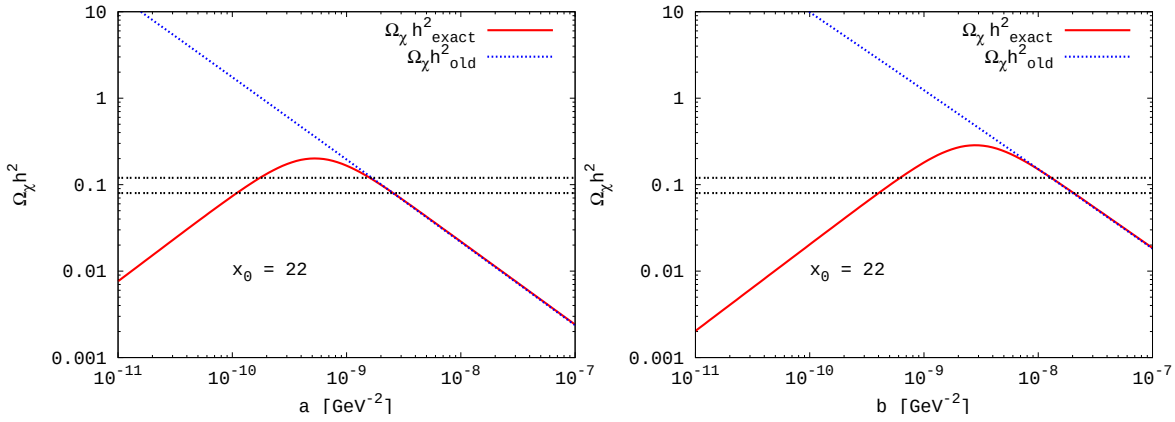

(a) (b)

Figure 4.1: Predicted present relic density $\Omega_\chi h^2$ as function of the a and b contributions to the total cross section, see Eq.(3.11); in frame (a), $b = 0$ whereas in (b), $a = 0$. We consider two extreme cases: χ particles were in full thermal equilibrium (dotted blue line) or the number density of χ vanished (solid red line) at $x_0 = 22$. The two horizontal double–dotted black lines correspond to the 2σ upper and lower bounds of the dark matter abundance [1].

are constants. Here we assume $g_* \simeq g_{*s}$ and $dg_{*s}/dx \simeq 0$. Eqs.(3.8) and (4.1) assume that χ remains in kinetic equilibrium through the entire period with non–negligible time dependence of Y_χ. This is reasonable, since kinetic equilibrium can be maintained through elastic scattering of χ particles on particles in the thermal plasma. The rate for such reactions exceeds the χ annihilation rate by a factor $\propto Y_\chi^{-1} \gtrsim 10^7$ for temperatures of interest. For our numerical examples, we consider a Majorana fermion with $m = 100$ GeV and $g_\chi = 2$ as the relic particle. We choose the relativistic degrees of freedom to be $g_* = 90$; this approximates the prediction of SM of particle physics for temperatures around 10 GeV.

Figure 4.1 shows that the relic density can be reduced if the particles never reach thermal equilibrium because of the low reheat temperature after inflation. The solid red curves depict the predicted present relic density $\Omega_\chi h^2$ as function of a (a) and b (b) defined in Eq.(3.11). Here we assume that the relic abundance vanished at the initial temperature of $x_0 = 22$, which is around the typical WIMP decoupling temperature. Here, as well as in the subsequent figures, the exact numerical solution of the Boltzmann equation (4.1) has been obtained using the Runge–Kutta algorithm, with a step size that increases quickly with increasing $x - x_0$. For large cross section we observe $\Omega_\chi h^2 \propto 1/\langle\sigma v\rangle$, in accord with the

standard prediction (3.18). However, when the cross section is reduced, the relic density reaches a maximum, and then decreases $\propto \langle\sigma v\rangle$. For the given choice of initial conditions, there are therefore two distinct ranges in $\langle\sigma v\rangle$ where the relic density comes out in the desired range [1]. In the following section, we calculate the relic abundance in analytic way.

4.2 Analytic Calculation of Relic Abundance

We calculated the relic density in approximate way in the standard cosmological scenario. In the following we attempt to find a convenient approximate analytic formula applicable even to low temperature scenarios. As zeroth order solution of Eq.(4.1) we consider the case where χ annihilation is completely negligible,

$$\frac{dY_0}{dx} = fc(ax + 6b)\,\mathrm{e}^{-2x}\,. \tag{4.3}$$

This equation can easily be integrated, giving

$$Y_0(x) = fc\left[\frac{a}{2}(x_0\mathrm{e}^{-2x_0} - x\mathrm{e}^{-2x}) + \left(\frac{a}{4} + 3b\right)(\mathrm{e}^{-2x_0} - \mathrm{e}^{-2x})\right] + Y_\chi(x_0)\,. \tag{4.4}$$

For $x \gg x_0$, the relic abundance of the particles becomes constant,

$$Y_{0,\infty} \equiv Y_0(x \gg x_0) = fc\left[\frac{a}{2}x_0\mathrm{e}^{-2x_0} + \left(\frac{a}{4} + 3b\right)\mathrm{e}^{-2x_0}\right] + Y_\chi(x_0)\,. \tag{4.5}$$

It can be simplified by putting the constants f and c into $Y_0(x)$ and let $Y_\chi(x_0) = 0$,

$$Y_{0,\infty} \simeq 0.014 g_\chi^2 g_*^{-3/2} m_\chi M_{\mathrm{Pl}}\mathrm{e}^{-2x_0}x_0(a + \frac{6b}{x_0}). \tag{4.6}$$

The corresponding prediction for the present relic density is given by

$$\begin{aligned}\Omega_\chi h^2 &= 2.8\times 10^8 m_\chi Y_{0,\infty}\mathrm{GeV}^{-1} \\ &= 3.9\times 10^6 g_\chi^2 g_*^{-3/2} m_\chi^2 M_{\mathrm{Pl}}\mathrm{e}^{-2x_0}x_0(a + \frac{6b}{x_0})\ \mathrm{GeV}^{-1}.\end{aligned} \tag{4.7}$$

Here we notice that the relic density is proportional to the cross section, although the coefficient of proportionality depends on whether a or b is dominant. The final abundance is found to be enhanced as the cross section or the initial temperature increases. This solution should be smoothly connected to the one which is obtained in the full thermal equilibrium case.

So far no analytic solution has been known for the in–between case where both annihilation and production play a crucial role in determining the relic abundance while thermal equilibrium is not fully achieved. We now attempt to connect the standard scenario ($T_R > T_F$) and the low reheat temperature scenario ($T_R < T_F$) using some analytic method.

Since we already have the solution only including the production term, the most natural extension is to add a correction term which describes the effect of annihilation on the solution for the pure production case:

$$Y_1 = Y_0 + \delta\,. \tag{4.8}$$

By definition δ vanishes at the initial temperature. Since it describes the effect of χ annihilation, it is negative for $x > x_0$. We put Eq.(4.8) into Eq.(4.1),

$$\frac{d(Y_0+\delta)}{dx} = -f\left(a+\frac{6b}{x}\right)\frac{1}{x^2}\left[(Y_0+\delta)^2 - cx^3\mathrm{e}^{-2x}\right]\,. \tag{4.9}$$

As long as $|\delta|$ is small compared to Y_0, the evolution equation for δ is given by

$$\frac{d\delta}{dx} = -f\left(a+\frac{6b}{x}\right)\frac{Y_0(x)^2}{x^2}\,. \tag{4.10}$$

Using Eq.(4.4) for $Y_0(x)$, this can again be integrated:

$$\begin{aligned}\delta(x) &= -f^3c^2\left[\frac{1}{4}a^3F_0^4(x,x_0) + \frac{1}{4}a^2(a+18b)F_1^4(x,x_0)\right.\\ &\qquad \left. +\frac{1}{16}a(a+12b)(a+36b)F_2^4(x,x_0) + \frac{3}{8}b(a+12b)^2F_3^4(x,x_0)\right]\\ &+ Y_{0,\infty}f^2c\left[a^2F_1^2(x,x_0) + \frac{1}{2}a(a+24b)F_2^2(x,x_0) + 3b(a+12b)F_3^2(x,x_0)\right]\\ &- Y_{0,\infty}^2 f\left[aF_2^0(x,x_0) + 6bF_3^0(x,x_0)\right]\,,\end{aligned} \tag{4.11}$$

where

$$F_n^m(x,x_0) = \int_{x_0}^{x} dt\;\frac{\mathrm{e}^{-mt}}{t^n}\,,\quad m=0,2,4\,,\quad n=1,2,3\,. \tag{4.12}$$

The functions $F_n^m(x,x_0)$ can be expressed analytically in terms of the exponential integral of first order $\mathrm{E}_1(x)$; a complete list of the relevant F_n^m is given in the Appendix, Eqs.(A.6).

At late times, $x \to \infty$, this simplifies to

$$\begin{aligned}\delta(x\to\infty) &= -f^3c^2\mathrm{e}^{-4x_0}\left[\frac{a^3}{4}x_0+\frac{a^2(a+60b)}{16}-\frac{9ab(a-16b)}{8x_0}\right.\\ &\qquad\left.+\frac{9b(5a^2-56ab+96b^2)}{32x_0^2}\right]\\ &- f^2c\mathrm{e}^{-2x_0}Y_\chi(x_0)\left[a^2+\frac{9ab}{x_0}-\frac{9b(a-4b)}{2x_0^2}\right]\\ &- f(Y_\chi(x_0))^2\left(\frac{a}{x_0}+\frac{3b}{x_0^2}\right), \end{aligned} \tag{4.13}$$

where we omit higher order terms than $\mathcal{O}(1/x_0^2)$. Notice that we discard $\mathcal{O}(1/x^2)$ and $\mathcal{O}(1/x^3)$ terms in $\langle\sigma v\rangle$, which also contribute to higher order terms in Eq.(4.13). If $a \neq 0$ we therefore expect additional terms $\mathcal{O}(1/x_0)$ from terms not included in Eq.(3.11); if $a = 0$, higher order terms in the expansion of the cross section only contribute at $\mathcal{O}(1/x_0^3)$ in Eq.(4.13). With the vanishing initial abundance, it is simplified to

$$\delta(x\to\infty) \simeq -2.5\times10^{-4}\; g_\chi^4 g_*^{-5/2} m_\chi^3 M_{\mathrm{Pl}}^3 \mathrm{e}^{-4x_0} x_0 \left(a+\frac{3b}{x_0}\right)\left(a+\frac{6b}{x_0}\right)^2 . \tag{4.14}$$

We put the solutions for δ and Y_0 together to Y_1 and compare the approximate analytic result with the numerical one. We find there is little deviation when the cross section is small, the deviation increases fast when the cross section increases. Therefore, we try to find more useful analytic formula.

Since, for vanishing initial abundance, Y_0 is proportional to the cross section σ, δ is proportional to σ^3. On the other hand, for sufficiently large cross section we want to recover the standard expression, where $Y_\chi(x\to\infty) \propto 1/\langle\sigma v\rangle$. This suggests to rewrite our ansatz (4.8) as

$$Y_1 = Y_0 + \delta = Y_0\left(1+\frac{\delta}{Y_0}\right) \simeq \frac{Y_0}{1-\delta/Y_0} \equiv Y_{1,r}\,. \tag{4.15}$$

Although the final approximate equality in Eq.(4.15) only holds for $|\delta| \ll Y_0$, we note that the resulting expression has the right behavior, $Y_{1,r} \propto 1/\sigma$, for large cross section. In the following we will show that this "re–summation" of the correction δ is indeed able to describe the relic density for a wide range of cross sections and temperatures, including scenarios where the standard treatment is applicable.

In fact, this ansatz solves the Boltzmann equation (4.1) exactly in the simple case where

thermal χ production can be ignored, but $Y_\chi(x_0)$ is sizable, leading to significant χ annihilation. In this case Eq.(4.1) reduces to

$$\frac{dY_\chi}{dx} = -f\left(a + \frac{6b}{x}\right)\frac{Y_\chi^2}{x^2}\,. \tag{4.16}$$

This equation can easily be solved analytically. The solution decreases monotonically from its initial value $Y_\chi(x_0)$:

$$Y_\chi = \frac{Y_\chi(x_0)}{1 + fY_\chi(x_0)\left[a(1/x_0 - 1/x) + 3b(1/x_0^2 - 1/x^2)\right]}\,. \tag{4.17}$$

In order to treat this case using the formalism of Eqs.(4.3)–(4.15), we simply drop all terms which depend exponentially on x or x_0; these terms come from thermal χ production, and are obviously very small for sufficiently small initial temperature. The zeroth order solution (4.4) then obviously reduces to the constant $Y_\chi(x_0)$, and the correction δ of Eq.(4.11) simplifies to

$$\begin{aligned}\delta(x) &\rightarrow -f\left(Y_\chi(x_0)\right)^2\left[aF_2^0(x,x_0) + 6bF_3^0(x,x_0)\right] \\ &= -f\left(Y_\chi(x_0)\right)^2\left[a\left(\frac{1}{x_0} - \frac{1}{x}\right) + 3b\left(\frac{1}{x_0^2} - \frac{1}{x^2}\right)\right]\,;\end{aligned} \tag{4.18}$$

in the last step we have used the last two Eqs.(A.6) in the Appendix. Inserting this in the last expression in Eq.(4.15), we indeed recover the exact solution (4.17), as advertised.

In principle, we can add further correction terms to the first order approximation of Eq.(4.8),

$$Y_\chi = Y_0 + \delta + \delta_2 + \delta_3 + \cdots\,. \tag{4.19}$$

The above discussion shows that this corresponds to an expansion in powers of $\langle\sigma v\rangle$. Since $Y_0 > 0$ and $\delta < 0$ by definition, the systematic expansion will lead to an alternating series which possesses good convergence properties. However, this type of expansion is quite cumbersome because $|\delta|$ often dominates over Y_0 for not very small cross sections, as we will explicitly see later. Therefore the re–summed ansatz $Y_{1,r}$ of Eq.(4.15) is much more convenient. We will see that it often provides a good approximation to the exact solution even if thermal χ production is not negligible.

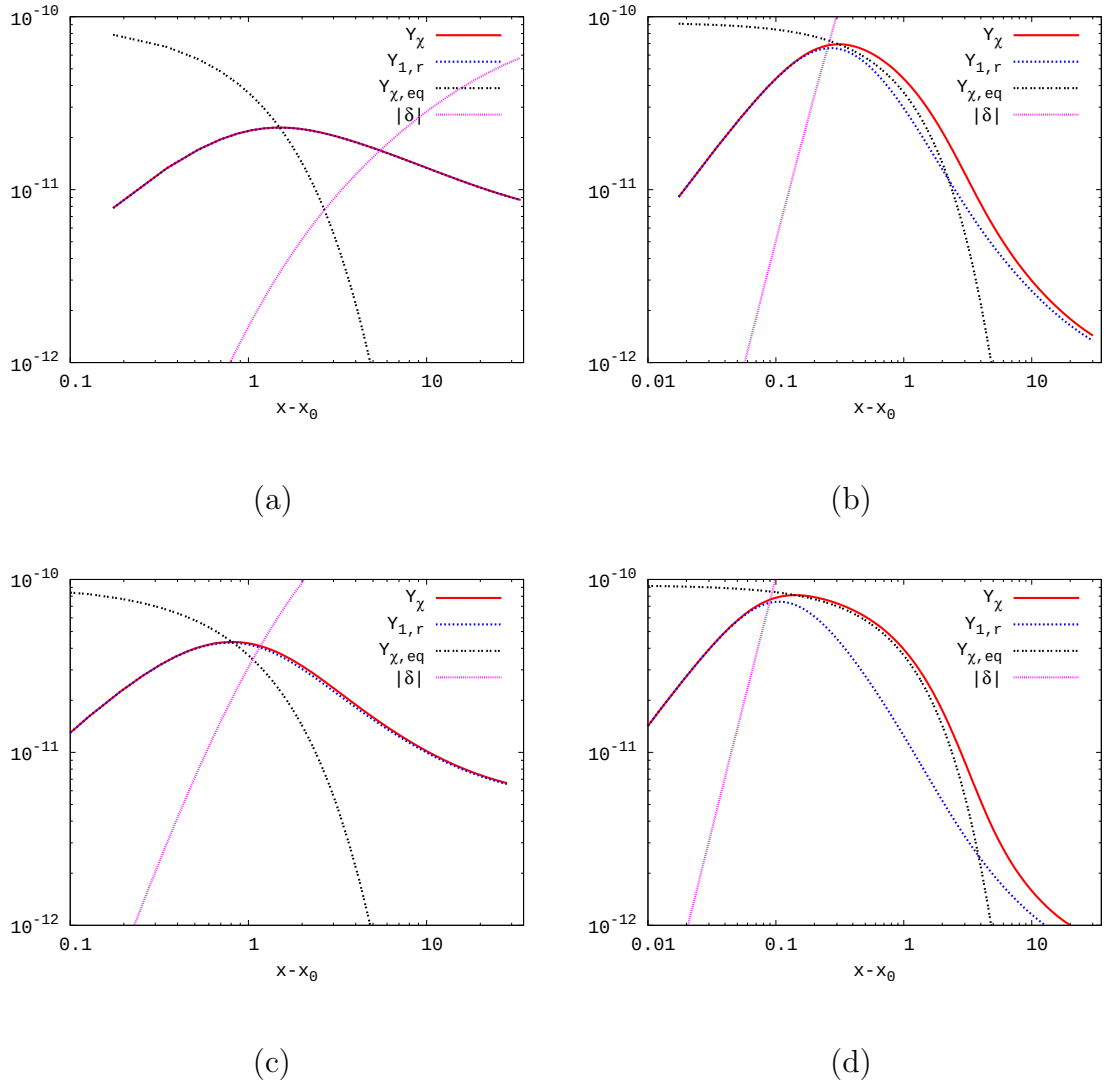

Figure 4.2: Evolution of the exact solution Y_χ (solid red curves), $Y_{1,r}$ of Eq.(4.15) (dotted blue), the equilibrium density $Y_{\chi,\mathrm{eq}}$ of Eq.(3.4) (double–dotted black), and $|\delta|$ of Eq.(4.11) (short–dashed violet) as function of $x - x_0$. The initial abundance is assumed to be $Y_\chi(x_0 = 22) = 0$. We take (a) $a = 10^{-9}$ GeV^{-2}, $b = 0$, (b) $a = 10^{-8}$ GeV^{-2}, $b = 0$, (c) $a = 0$, $b = 10^{-8}$ GeV^{-2}, and (d) $a = 0$, $b = 10^{-7}$ GeV^{-2}. In frames (a) and (c) the curves for $Y_{1,r}$ practically coincide with the solid lines.

In Fig. 4.2 we present the evolution of the exact, numerical solution Y_χ (solid red), $Y_{1,r}$ (dotted blue), $Y_{\chi,\mathrm{eq}}$ (double–dotted black) and $|\delta|$ (short–dashed violet) as function of $x - x_0$. Here we consider vanishing initial χ density, $Y_\chi(x_0 = 22) = 0$. Clearly the first order approximation Y_1 of Eq.(4.8) fails to reproduce the exact result once $|\delta|$ becomes comparable to Y_0. On the contrary, frames (a) and (c) show that the re–summed ansatz $Y_{1,r}$ of Eq.(4.15) reproduces the numerical solution very well for all $x > x_0$ if $a \lesssim 10^{-9}$

GeV^{-2} and $b \lesssim 10^{-8}$ GeV^{-2}. However, for intermediate values of $x - x_0$, the disagreement between $Y_{1,r}$ and the exact solution becomes large as the cross section increases. In frames (b) and (d) of Fig. 4.2 sizable deviations from the exact value are observed at $x - x_0 \sim 1$ for $a = 10^{-8}$ GeV^{-2} or $b = 10^{-7}$ GeV^{-2}. For larger x the deviation becomes smaller again, and for $x \gg x_0$ the difference is insignificant even for these large cross sections.

We also analyzed scenarios with sizable initial χ abundance, $Y_\chi(x_0) \neq 0$. Figure 4.3 shows that the re–summed ansatz again matches the numerical result very well for all values of x if $a \lesssim 10^{-9}$ GeV^{-2}. This is not surprising since, as we saw in the discussion of Eq.(4.18), it reproduces the exact solution if $Y_\chi(x_0)$ dominates over the thermal contribution. For $a = 10^{-8}$ GeV^{-2}, $Y_{1,r}$ again starts to deviate from the exact numerical solution at $x \sim 0.1$, but approaches it for $x \gg x_0$. Note also that already for the smaller cross section chosen in this Figure, the final relic density is almost independent of $Y_\chi(x_0)$.

Let us take a closer look at the difference between the exact solution and the re–summed ansatz. To this end, we define the deviation ϵ by

$$Y_\chi = \frac{Y_0}{1 - \delta/Y_0} + \epsilon \,. \tag{4.20}$$

Inserting this ansatz into the Boltzmann equation (3.8) leads to the evolution equation for ϵ:

$$\frac{d\epsilon}{dx} = -\frac{f\langle\sigma v\rangle}{x^2}\left[\epsilon^2 + 2\epsilon\,\frac{Y_0}{1-\delta/Y_0} - \frac{(\delta/Y_0)^2}{(1-\delta/Y_0)^2}\,Y_{\chi,\mathrm{eq}}^2\right], \tag{4.21}$$

which again resembles the Boltzmann equation. Since initially $\epsilon = 0$, our re–summed ansatz works very well as long as δ/Y_0 remains suppressed. Note that the inhomogeneous term on the rhs of Eq.(4.21) is of order $(\delta/Y_0)^2$. The analogous correction to our original first order solution Y_1 of Eq.(4.8) would start at $\mathcal{O}(\delta/Y_0)$. Since this inhomogeneous term is positive, $\epsilon(x) > 0$ for all $x > x_0$, i.e. $Y_{1,r}$, like Y_1, always under–estimates the exact solution. As $|\delta|/Y_0$ grows, the last term in Eq.(4.21) can become sizable. Note, however, that it is multiplied with $(Y_{\chi,\mathrm{eq}})^2$, which drops $\propto \exp(-2x)$ with increasing x. Therefore ϵ becomes large only if $|\delta|$ reaches values of order of Y_0 for $x - x_0 \lesssim 1$. The homogeneous terms in Eq.(4.21) imply that for large $x - x_0$ the deviation ϵ decreases again, similar to the WIMP relic abundance Y_χ. This situation is depicted in Fig. 4.4, which shows the evolutions of $|\delta|/Y_\chi$ (upper curves) and ϵ/Y_χ (lower curves) as function of $x - x_0$ for $a = 3 \times 10^{-8}$ GeV^{-2} (solid red), $a = 10^{-8}$ GeV^{-2} (dotted blue) and $a = 3 \times 10^{-9}$ GeV^{-2} (double–dotted black). Here we choose $b = 0$ and $Y_\chi(x_0 = 22) = 0$. Even in the case where

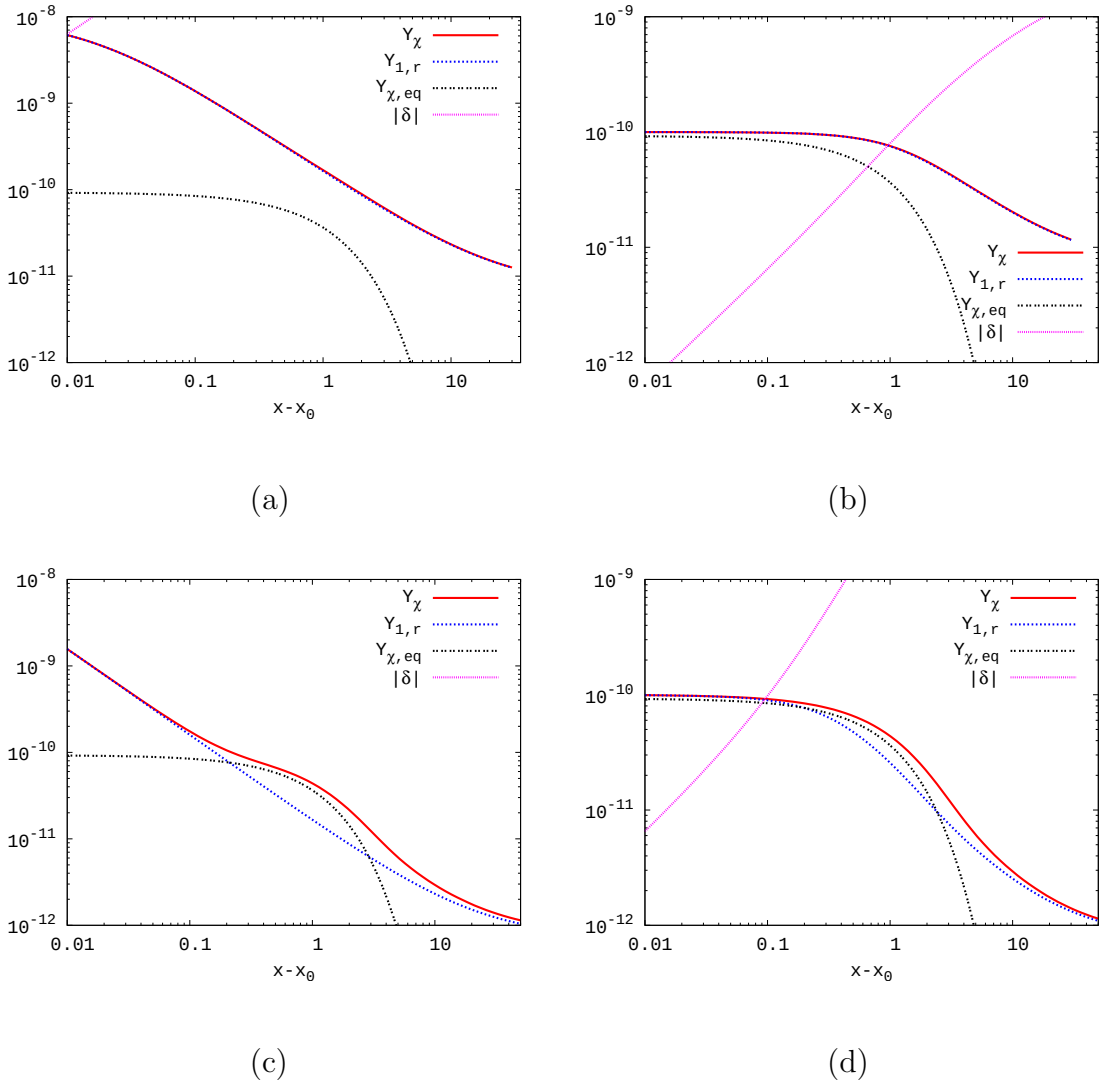

Figure 4.3: Evolution of Y_χ (solid red curves), $Y_{1,r}$ (dotted blue), $Y_{\chi,\mathrm{eq}}$ (double–dotted black) and $|\delta|$ (short–dashed violet) as function of $x-x_0$. Here we take (a) $a = 10^{-9}$ GeV^{-2}, $Y_\chi(x_0) = 10^{-8}$, (b) $a = 10^{-9}$ GeV^{-2}, $Y_\chi(x_0) = 10^{-10}$, (c) $a = 10^{-8}$ GeV^{-2}, $Y_\chi(x_0) = 10^{-7}$ and (d) $a = 10^{-8}$ GeV^{-2}, $Y_\chi(x_0) = 10^{-10}$. The other parameters are as in Fig. 4.2.

ϵ becomes sizable for intermediate values of x, it eventually diminishes and hence our analytical formula succeeds in reproducing the present relic abundance $Y_\chi(x \to \infty)$ fairly well.

Following we discuss the dependence of the present relic abundance on the initial temperature. In Fig. 4.5 we plot the present relic density evaluated numerically (solid red curves), the old standard approximation (dotted blue) and our new approximation (double–dotted

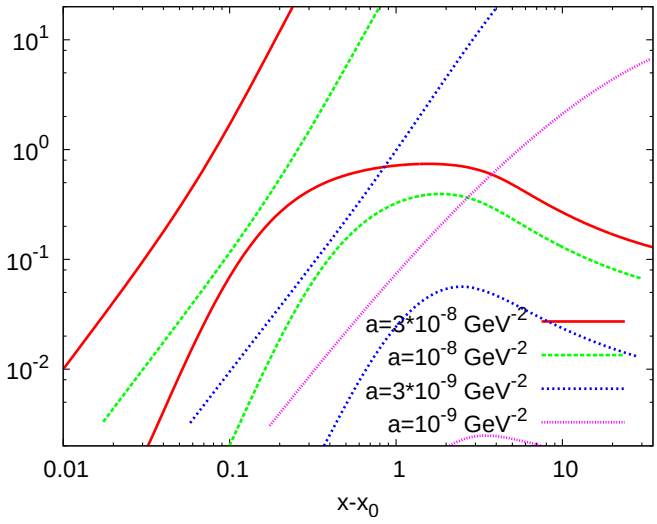

Figure 4.4: Evolution of $|\delta|/Y_\chi$ (upper curves) and ϵ/Y_χ (lower curves) as function of $x - x_0$ for $a = 3 \times 10^{-8}$ GeV^{-2} (solid red), $a = 10^{-8}$ GeV^{-2} (dotted blue) and $a = 3 \times 10^{-9}$ GeV^{-2} (double–dotted black). Here we choose $b = 0$ and $Y_\chi(x_0 = 22) = 0$.

black) as function of x_0. Here we take (a) $a = 10^{-8}$ GeV^{-2}, $b = 0$ and (b) $a = 10^{-9}$ GeV^{-2}, $b = 0$. We find that our approximation agrees with the exact result very well for $x_0 > x_F$. On the other hand, for $x_0 < x_F$, our approximation gives too small an abundance[1] while the old approximation works very well. The transition between the two regimes is very sharp. For $x_0 = x_F + 2$, the old approximation over–estimates the relic abundance by as much as an order of magnitude, while for $x_0 = x_F$ both the old and the new approximation work well.

Fig. 4.5 shows that $Y_{1,r}(x_0, x \to \infty)$ has a well defined maximum when x_0 is varied. This maximum occurs at a value $x_{0,\max}$ which is close, but not identical, to the decoupling temperature x_F of Eq.(3.20). From the asymptotic expressions for Y_0, Eq.(4.5), and δ, Eq.(4.13), we find for $Y_\chi(x_0) = 0$:

$$\begin{aligned} x_{0,\max} &\simeq \frac{1}{2} \ln \frac{f^2 c (a + 6b/x_{0,\max})^2}{4 x_{0,\max}} \\ &= \ln \frac{0.096 \; m_\chi M_{\rm Pl} g_\chi (a + 6b/x_{0,\max})}{\sqrt{x_{0,\max} g_*}} \,. \end{aligned} \tag{4.22}$$

[1] For $x_0 \ll x_F$, our expressions predict $\Omega_\chi h^2 \propto x_0$.

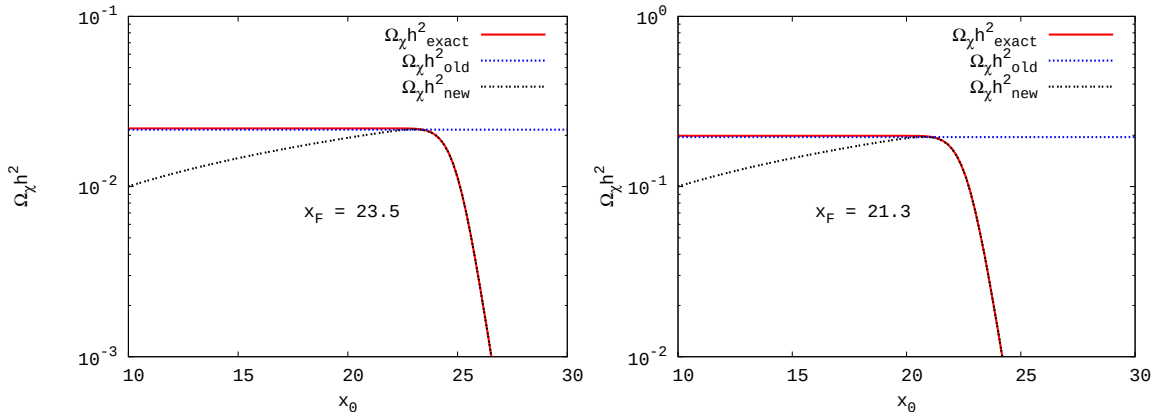

(a) (b)

Figure 4.5: The present relic density evaluated numerically (solid red curves), the old standard approximation (dotted blue) and our new approximation (double–dotted black) as function of x_0. Here we take (a) $a = 10^{-8}$ GeV^{-2}, $b = 0$ and (b) $a = 10^{-9}$ GeV^{-2}, $b = 0$.

In deriving this equation, we neglect non–leading terms in $1/x_{0,\max}$ in each combination of a and b.[2] Notice that $x_{0,\max}$ coincides with x_F of Eq.(3.20), if one chooses $\xi = 1/4$ (rather than $\xi = \sqrt{2} - 1$).

Since the actual relic density is already practically independent of x_0 for $x_0 < x_{0,\max}$, we can construct a new semi–analytic solution which describes the relic density for the whole range of x_0: for $x_0 > x_{0,\max}$, compute the relic density from $Y_{1,r}(x_0)$, but for $x_0 < x_{0,\max}$, use $Y_{1,r}(x_{0,\max})$ instead.

The ratio of this semi–analytic result $\Omega_{1,r}$ to the exact value Ω_χ is depicted in Fig. 4.6. As noted earlier, our approximation becomes exact for $x_0 \gtrsim x_F$. For smaller x_0 the new approximation still slightly under–estimates the correct answer, but the deviation is at most 1.7% for $b = 0$ (left frame), and 3.0% for $a = 0$ (right frame). On the other hand, in the same region the old standard approximation reproduces the present relic abundance within 1% error. We thus see that for $x_0 < x_F$, this new expression works nearly as well as the old standard result;[3] of course, the old result fails badly for $x_0 > x_F$. Finally, since

[2]The next–to–leading correction to the pure a–term would have been relevant, but it cancels. The non–leading corrections to terms that require both a and b to be non–zero are numerically insignificant, and of the same order as terms omitted in the expansion (3.11) of the annihilation cross section.

[3]However, if $a = 0$, we should expect $\mathcal{O}(10\%)$ corrections to the relic density from higher order terms in

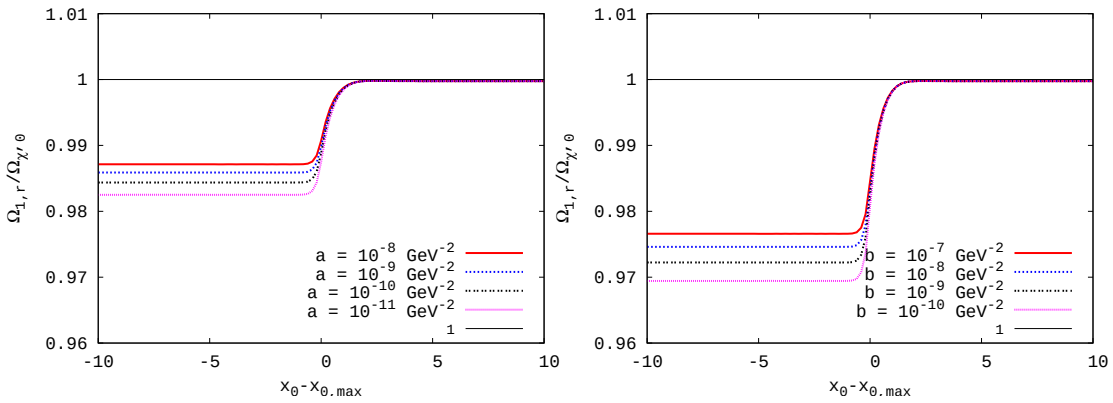

(a) (b)

Figure 4.6: Ratios of approximate and exact results for the relic density $\Omega_{1,r}/\Omega_\chi$ as function of $x_0 - x_{0,\max}$, for $a \neq 0$, $b = 0$ (left frame) and $a = 0, b \neq 0$ (right frame). The curves use $Y_{1,r}$ with x_0 replaced by $\max(x_0, x_{0,\max})$, see Eq.(4.22). In the left frame, $a = 10^{-8}$ GeV^{-2} (solid red curves), 10^{-9} GeV^{-2} (dotted blue), 10^{-10} GeV^{-2} (double–dotted black), 10^{-11} GeV^{-2} (short–dashed violet) with $b = 0$, whereas in the right frame, $b = 10^{-7}$ GeV^{-2} (solid red), 10^{-8} GeV^{-2} (dotted blue), 10^{-9} GeV^{-2} (double–dotted black), 10^{-10} GeV^{-2} (short–dashed violet) with $a = 0$.

by definition $Y_{1,r}$ depends only weakly on x_0 for $x_0 \sim x_{0,\max}$, the latter quantity need not be calculated very precisely; in practice, setting $x_{0,\max} = 20$ in the rhs of Eq.(4.22) is often sufficient. In contrast, the standard approximation (3.18) depends linearly (for $b = 0$) or even quadratically (for $a = 0$) on x_F; several iterations are therefore required to solve Eq.(3.20) to sufficient accuracy. Altogether, our new semi–analytic formula is evidently a quite powerful tool in calculating the density of cold relics.

4.3 Constraint on Initial Temperature from Dark Matter Relic Abundance

In the previous sections, we explore the relic density of WIMPs in the low–temperature scenario. Bearing the behavior of the final relic abundance in mind, it is worth to investigate its dependence on the initial temperature T_0. With the precisely measured abundance of cold dark matter in the universe we can derive the possible lowest initial temperature if cold dark matter is mainly composed of thermally produced WIMPs [36]. Some results

the expansion (3.11) of the cross section; if $a \neq 0$, these higher order terms should only contribute $\mathcal{O}(1\%)$.

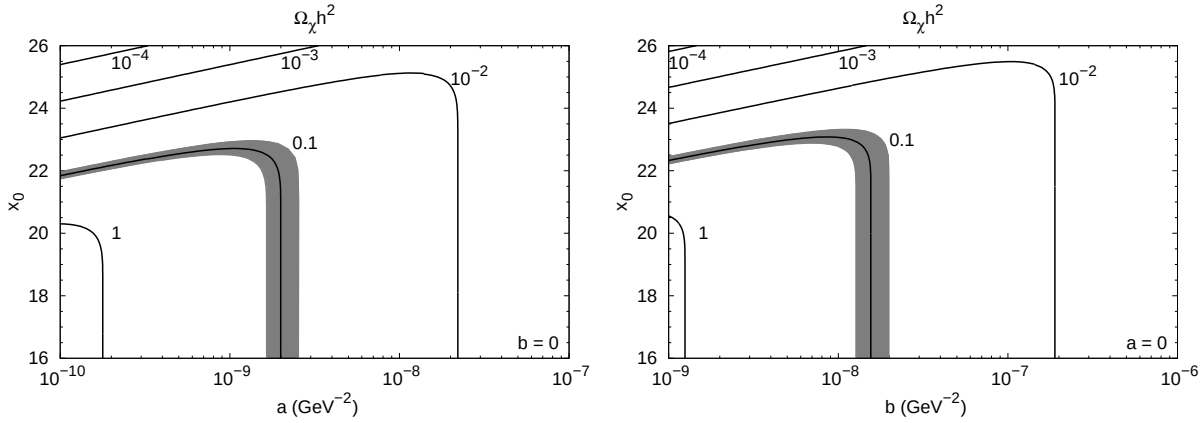

(b)

Figure 4.7: Contour plots of the present relic abundance $\Omega_\chi h^2$. Here we take (a) $a \neq 0, b = 0$, and (b) $a = 0, b \neq 0$. We choose $Y_\chi(x_0) = 0$, $m_\chi = 100$ GeV, $g_\chi = 2$, $g_* = 90$. The shaded region corresponds to the WMAP bound on the cold dark matter abundance, $0.08 < \Omega_{\mathrm{CDM}} h^2 < 0.12$ (95% C.L.).

are shown in Fig. 4.7, where we take (a) $a \neq 0, b = 0$, and (b) $a = 0, b \neq 0$. We choose $Y_\chi(x_0) = 0$, $m_\chi = 100$ GeV, $g_\chi = 2$ and $g_* = 90$.

The results depicted in this Figure can be understood as follows. For small T_0, i.e. large x_0, Eq.(4.6) is valid, leading to a very strong dependence of $\Omega_\chi h^2$ on x_0. Recall that in this case the relic density is proportional to the cross section. In this regime one can reproduce the relic density (1.1) with quite small annihilation cross section, $a + 6b/x_0 \lesssim 10^{-9}$ GeV^{-2}, for some narrow range of initial temperature, $x_0 \lesssim 22.5$. Note that this allows much smaller annihilation cross sections than the standard result, at the cost of a very strong dependence of the final result on the initial temperature T_0.

In this Section we set out to derive a lower bound on T_0. In this regard the region of parameter space described by Eq.(4.6) is not optimal. Increasing the χ annihilation cross section at first allows to obtain the correct relic density for larger x_0, i.e. smaller T_0. However, the correction δ then quickly increases in size; as noted earlier, once $|\delta| > Y_0$ a further increase of the cross section will lead to decrease of the final relic density. The lower bound on T_0 is therefore saturated if $\Omega_\chi h^2$ as a function of the cross section reaches a maximum.

From Fig.4.7 we read off

$$T_0 \geq m_\chi/23\,, \tag{4.23}$$

if we require $\Omega_\chi h^2$ to fall in the range (1.1).

We just saw that in the regime where this bound is saturated, the final relic density is (to first order) independent of the annihilation cross section, $\partial(\Omega_\chi h^2)/\partial\langle\sigma v\rangle = 0$. If T_0 is slightly above the absolute lower bound (4.23), the correct relic density can therefore be obtained for a rather wide range of cross sections. For example, if $x_0 = 22.5$, the entire range 3×10^{-10} GeV$^{-2} \lesssim a \lesssim 2 \times 10^{-9}$ GeV^{-2} is allowed. Of course, the correct relic density can also be obtained in the standard scenario of (arbitrarily) high T_0, if $a + 3b/22$ falls within $\sim 20\%$ of 2×10^{-9} GeV^{-2}.

Chapter 5

Relic Abundance Including Non–thermal Production

In this chapter we investigate a scenario where unstable heavy particles ϕ decay into long–lived or stable particles χ. We assume that ϕ decays out of thermal equilibrium, so that ϕ production is negligible; however, we include both thermal and non–thermal production of χ particles. For example in some supersymmetric models neutralinos can be produced non–thermally through the decay of moduli [30] or gravitinos after the end of inflation. This chapter is devoted to the calculation of the relic density of WIMPs including the decay of heavier particles.

5.1 The Boltzmann Equation

The evolution of the cosmological abundance including the decay of heavier particle is more complicated than in the usual thermal–production case reviewed in the previous chapter. The number densities of χ and ϕ obey the following coupled Boltzmann equations:

$$\begin{aligned} \frac{dn_\chi}{dt} + 3Hn_\chi &= -\langle\sigma v\rangle(n_\chi^2 - n_{\chi,\mathrm{eq}}^2) + N\Gamma_\phi n_\phi \,, \\ \frac{dn_\phi}{dt} + 3Hn_\phi &= -\Gamma_\phi n_\phi \,, \end{aligned} \tag{5.1}$$

where N is the average number of χ particles produced in a ϕ decay, and Γ_ϕ and n_ϕ are the decay rate and the number density of the heavier particle. In contrast to refs. [19] we assume that ϕ does not dominate the total energy density, so that the co–moving entropy density remains approximately constant throughout. The Boltzmann equation for n_ϕ can then easily be solved analytically, using the fact that $t \propto T^{-2} \propto x^2$ in the radiation–dominated

era. Inserting this solution into the equation for n_χ, and again switching variables to $Y_\chi = n_\chi/s$, $Y_\phi = n_\phi/s$ and x, the Boltzmann equation for χ becomes

$$\frac{dY_\chi}{dx} = -\frac{\langle\sigma v\rangle s}{Hx}(Y_\chi^2 - Y_{\chi,\mathrm{eq}}^2) + NrxY_\phi(x_0)\exp\left(-\frac{r}{2}(x^2 - x_0^2)\right) , \tag{5.2}$$

where $r = \Gamma_\phi/Hx^2 = (\Gamma_\phi M_{\mathrm{Pl}}/\pi m_\chi^2)\sqrt{90/g_*}$ is constant. Comparing to the Boltzmann equation (4.1), there is extra term which emerged from the decay of heavier particles to WIMPs. The analytic approximate way which we used in the previous chapter also works for this case, but the calculation is more complicated than before.

5.2 Analytic Calculation of Relic Abundance

We repeat the same way as in Chapter 4 to solve the Boltzmann equation (5.2) approximately. The zeroth order solution of Eq.(5.2) is again obtained by neglecting χ annihilation when the temperature is too low for χ particle to reach thermal equilibrium. Using the expansion (3.11) of the annihilation cross section, we have

$$\frac{dY_0}{dx} = f\left(a + \frac{6b}{x}\right)cx\mathrm{e}^{-2x} + NrxY_\phi(x_0)\exp\left(-\frac{r}{2}(x^2 - x_0^2)\right) . \tag{5.3}$$

This equation can be integrated, giving

$$\begin{aligned} Y_0 &= fc\left[\frac{a}{2}(x_0\mathrm{e}^{-2x_0} - x\mathrm{e}^{-2x}) + \left(\frac{a}{4} + 3b\right)(\mathrm{e}^{-2x_0} - \mathrm{e}^{-2x})\right] \\ &+ NY_\phi(x_0)\left[1 - \exp\left(-\frac{r}{2}(x^2 - x_0^2)\right)\right] + Y_\chi(x_0) . \end{aligned} \tag{5.4}$$

For $x \gg x_0$, Y_0 becomes constant,

$$Y_{0,\infty} = fc\left[\frac{a}{2}x_0\mathrm{e}^{-2x_0} + \left(\frac{a}{4} + 3b\right)\mathrm{e}^{-2x_0}\right] + NY_\phi(x_0) + Y_\chi(x_0) . \tag{5.5}$$

For sufficiently large Y_0 the annihilation term in Eq.(5.2) becomes significant. We add a correction term to include this effect, as in Eq.(4.8). Since the new, non–thermal contribution to χ production is already fully included in Y_0, the Boltzmann equation for δ is again

given by Eq.(4.10). Using now Eq.(5.4) for Y_0, we can integrate Eq.(4.10), giving

$$\begin{aligned}
\delta &= \Big\{ -f^3 c^2 \left[\frac{1}{4} a^3 F_0^4(x,x_0) + \frac{1}{4} a^2 (a+18b) F_1^4(x,x_0) \right. \\
&\qquad \left. + \frac{1}{16} a(a+12b)(a+36b) F_2^4(x,x_0) + \frac{3}{8} b(a+12b)^2 F_3^4(x,x_0) \right] \\
&\quad + Y_{0,\infty} f^2 c \left[a^2 F_1^2(x,x_0) + \frac{1}{2} a(a+24b) F_2^2(x,x_0) + 3b(a+12b) F_3^2(x,x_0) \right] \\
&\quad - Y_{0,\infty}^2 f \left[a F_2^0(x,x_0) + 6b F_3^0(x,x_0) \right] \Big\} \\
&- N^2 Y_\phi^2(x_0) \mathrm{e}^{r x_0^2} f [a G_2^r(x,x_0) + 6b G_3^r(x,x_0)] \\
&+ 2N Y_\phi(x_0) \mathrm{e}^{r x_0^2/2} Y_{0,\infty} f [a G_2^{r/2}(x,x_0) + 6b G_3^{r/2}(x,x_0)] \qquad (5.6) \\
&- N Y_\phi(x_0) \mathrm{e}^{r x_0^2/2} f^2 c \left[a^2 G_1^c(x,x_0) + \frac{1}{2} a(a+24b) G_2^c(x,x_0) + 3b(a+12b) G_3^c(x,x_0) \right] .
\end{aligned}$$

The functions $G_n^r(x,x_0)$, $G_n^{r/2}(x,x_0)$ and $G_n^c(x,x_0)$ are defined by

$$\begin{aligned}
G_n^r(x,x_0) &= \int_{x_0}^x dt \, \frac{\mathrm{e}^{-rt^2}}{t^n} , \quad n = 2,3 , \\
G_n^{r/2}(x,x_0) &= \int_{x_0}^x dt \, \frac{\mathrm{e}^{-rt^2/2}}{t^n} , \quad n = 2,3 , \\
G_n^c(x,x_0) &= \int_{x_0}^x dt \, \frac{\mathrm{e}^{-2t-rt^2/2}}{t^n} , \quad n = 1,2,3 . \qquad (5.7)
\end{aligned}$$

Explicit expressions for these functions are given in the Appendix, Eqs.(A.8). Notice that the expression in curly brackets {...} in Eq.(5.6) has the same form as in Eq.(4.11).

Results for this scenario with $b = 0$ are shown in Fig. 5.1. We choose $r = 0.1$ so that $r x_0^2 \sim x_0$, which leads to the most difficult situation where thermal and non–thermal production occur simultaneously. We see that even for the smaller cross section considered, $a = 10^{-9}$ GeV^{-2} (top frames), the simple first–order solution (4.8) soon fails, since $|\delta|$ exceeds Y_0. However, the re–summed ansatz $Y_{1,r}$ of Eq.(4.15) describes the exact temperature dependence very well for this cross section, both for large (top left frame) and moderate (top right) non–thermal χ production. For $a = 10^{-8}$ GeV^{-2} (bottom frames) we again observe sizable deviations for intermediate values of $x - x_0$.

In fact, comparison with Fig. 4.2 shows that non–thermal χ production leads to faster growth of $|\delta|$, and hence to earlier and larger deviation between $Y_{1,r}$ and the exact solution

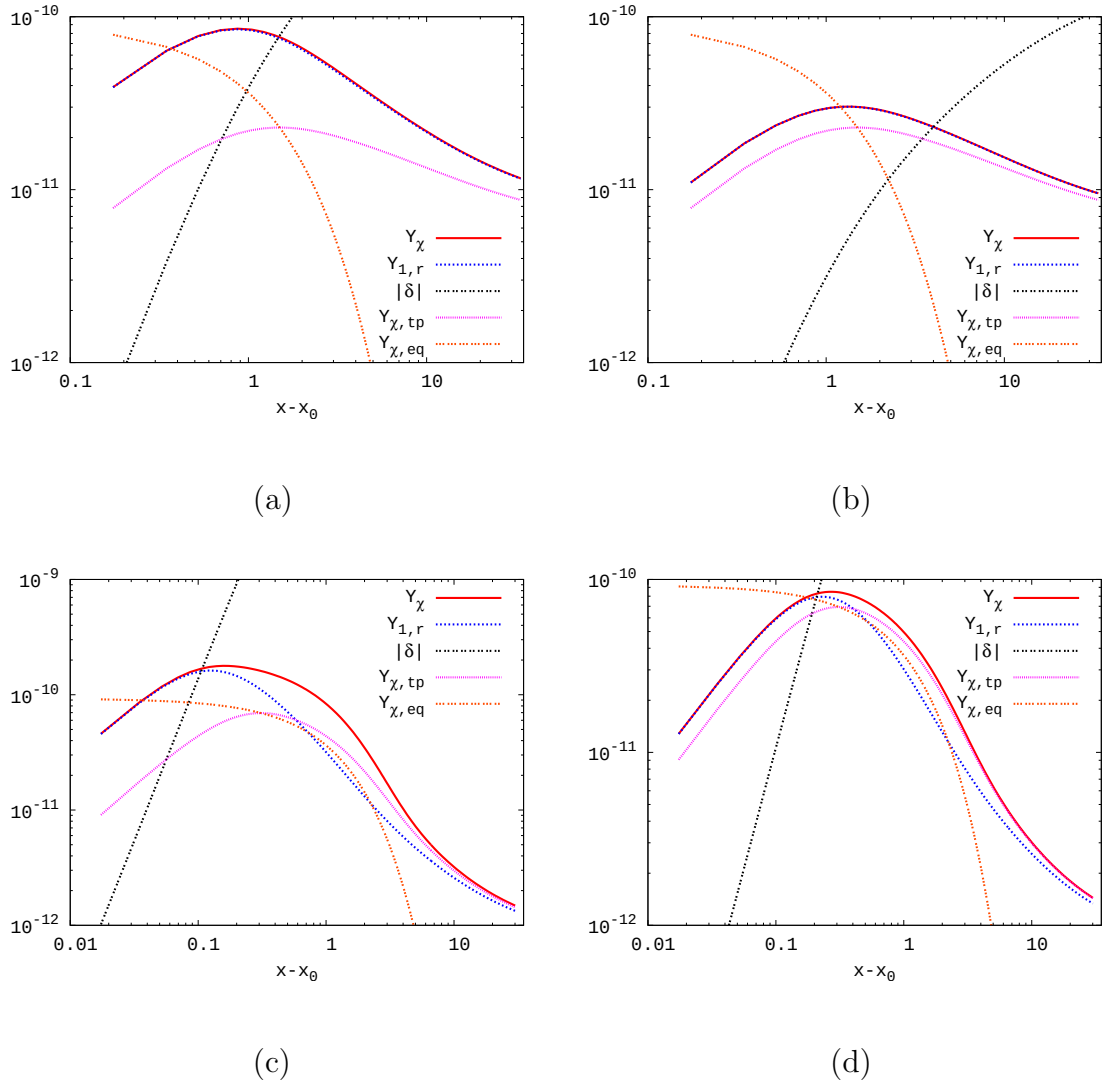

Figure 5.1: Evolution of Y_χ (solid red curves), $Y_{1,r}$ (dotted blue), $|\delta|$ (double–dotted black), the prediction for purely thermal χ production $Y_{\chi,\mathrm{tp}}$ (short–dashed violet) and $Y_{\chi,\mathrm{eq}}$ (triple–dotted orange) as function of $x - x_0$, for $Y_\chi(x_0 = 22) = 0$, $r = 0.1$, $N = 1$ and $b = 0$. The $S-$wave cross section and the initial ϕ density are (a) $a = 10^{-9}$ GeV^{-2}, $Y_\phi(x_0) = 10^{-10}$, (b) $a = 10^{-9}$ GeV^{-2}, $Y_\phi(x_0) = 10^{-11}$, (c) $a = 10^{-8}$ GeV^{-2}, $Y_\phi(x_0) = 10^{-9}$ and (d) $a = 10^{-8}$ GeV^{-2}, $Y_\phi(x_0) = 10^{-10}$.

of the Boltzmann equation (5.2). However, comparison with the curves labeled $Y_{\chi,\mathrm{tp}}$, where non–thermal χ production is neglected, show that for this rather large cross section and short ϕ lifetime, the non–thermal production mechanism does not affect the final χ relic density any more. This agrees with the result of Fig. 4.3, where we saw that for the same values of a and x_0, the relic density is independent of the initial value $Y_\chi(x_0)$. As before, $Y_{1,r}$ approaches the exact result again for $x - x_0 \gg 1$. We therefore conclude that our

re–summed ansatz describes scenarios with additional non–thermal χ production as well as the simpler case with only thermal production.

Chapter 6

Relic Abundance for the Modified Expansion Rate

In previous chapters we investigated the relic abundance in low–temperature scenarios. We find that different cosmological scenarios lead to different quantitive predictions for the relic density. In this chapter we investigate the relic abundance of WIMPs with the modified Hubble parameter. The influence of the modified expansion rate on the relic abundance of WIMP dark matter deserves to be studied for distinguishing among different cosmological scenarios. Various cosmological models predict a non–standard early expansion history [32–35]. Here we analyze to what extent the relic density of WIMP Dark Matter can be used to constrain the Hubble parameter during the epoch of WIMP decoupling [36]. As long as we assume large T_0 we can use a modification of the standard treatment [2, 14] to estimate the relic density for given annihilation cross section and expansion rate. We will show that the resulting approximate solutions again accurately reproduce the numerically evaluated relic abundance.

6.1 Boltzmann Equation and Relic Abundance

In this section we discuss the calculation of the WIMP relic density n_χ in modified cosmological scenarios where the expansion parameter of the pre–BBN universe differed from the standard value $H_{\rm st}$ of Eq.(3.9). For most part we will assume that WIMPs have been in full thermal equilibrium. We introduce the modification parameter $A(x)$, which parameterizes the ratio of the standard Hubble parameter $H_{st}(x)$ to the assumed $H(x)$:

$$A(x) = \frac{H_{st}(x)}{H(x)}. \tag{6.1}$$

We notice that $A > 1$ means that the expansion rate is smaller than in standard cosmology. Allowing for this modified expansion rate, the Boltzmann equation (3.8) is altered to

$$\frac{dY_\chi}{dx} = \frac{4\pi}{\sqrt{90}} G(x) m_\chi M_{\rm Pl} \frac{\langle\sigma v\rangle A(x)}{x^2} (Y^2 - Y^2_{\chi,\rm eq}). \tag{6.2}$$

The equation can be solved approximately in the same way which is reviewed in the standard cosmological scenario. We obtain the relic abundance as

$$Y_{\chi,\infty} \equiv Y_\chi(x \to \infty) = \frac{1}{(4\pi/\sqrt{90}) m_\chi M_{\rm Pl} I(x_F)}, \tag{6.3}$$

where the annihilation integral is defined as

$$I(x_F) = \int_{x_F}^{\infty} dx \frac{G(x)\langle\sigma v\rangle A(x)}{x^2}. \tag{6.4}$$

Plugging in numerical values for the Planck mass and for today's entropy density, the present relic density can thus be written as

$$\Omega_\chi h^2 = \frac{8.5 \times 10^{-11}}{I(x_F)\ \text{GeV}^2}. \tag{6.5}$$

The constraint (1.1) therefore corresponds to the allowed range for the annihilation integral

$$7.1 \times 10^{-10}\ \text{GeV}^{-2} < I(x_F) < 1.1 \times 10^{-9}\ \text{GeV}^{-2}\,. \tag{6.6}$$

The standard formula (3.18) for the final relic abundance is recovered if $A(x)$ is set to be unity and $G(x)$ is replaced by the constant $\sqrt{g_*(x_F)}$. The modification of the expansion parameter is encoded into the annihilation integral. Using the same method reviewed in Chapter 2, we find the freeze–out point as

$$x_F = \ln\left[\sqrt{\frac{45}{\pi^5}} \xi m_\chi g_\chi \frac{\langle\sigma v\rangle A(x)}{\sqrt{x g_*(x)}} \left(1 - \frac{x}{3 g_{*s}} \frac{dg_{*s}}{dx}\right)\right]\Bigg|_{x=x_F}, \tag{6.7}$$

which can e.g. be solved iteratively. In our numerical calculations we will choose $\xi = \sqrt{2}-1$ [2, 14].

The further discussion is simplified if we use the normalized temperature $z = T/m_\chi \equiv 1/x$, rather than x. Phenomenologically $A(z)$ can be any function subject to the condition that $A(z)$ approaches unity at late times in order not to contradict the successful predictions of BBN. We need to know $A(z)$ only for the interval from around the freeze-out to BBN:

$z_{\rm BBN} \sim 10^{-5} - 10^{-4} \lesssim z \lesssim z_F \sim 1/20$. This suggests a parameterization of $A(z)$ in terms of a power series in $(z - z_{F,\rm st})$:

$$A(z) = A(z_{F,\rm st}) + (z - z_{F,\rm st})A'(z_{F,\rm st}) + \frac{1}{2}(z - z_{F,\rm st})^2 A''(z_{F,\rm st})\,, \tag{6.8}$$

where $z_{F,\rm st}$ is the normalized freeze–out temperature in the standard scenario and a prime denotes a derivative with respect to z. The ansatz (6.8) should be of quite general validity, so long as the modification of the expansion rate is relatively modest. This suits our purpose, since we wish to find out what constraints can be derived on the expansion history if standard cosmology leads to the correct WIMP relic density.

We further introduce the variable

$$k = A(z \to 0) = A(z_{F,\rm st}) - z_{F,\rm st}A'(z_{F,\rm st}) + \frac{1}{2}z_{F,\rm st}^2 A''(z_{F,\rm st})\,, \tag{6.9}$$

which describes the modification parameter at late times. Since $z_{\rm BBN}$ is almost zero, we treat k as the modification parameter at the era of BBN in this paper.[1] Deviations from $k = 1$ are conveniently discussed in terms of the equivalent number of light neutrino degrees of freedom N_ν. BBN permits that the number of neutrinos differs from the standard model value $N_\nu = 3$ by $\delta N_\nu = 1.5$ or so [87]. We therefore take the uncertainty of k to be 20%. In the following we treat $A(z_{F,\rm st})$, $A'(z_{F,\rm st})$ and k as free parameters; $A''(z_{F,\rm st})$ is then a derived quantity.

Note that we allow $A(z)$ to cross unity, i.e. to switch from an expansion that is faster than in standard cosmology to a slower expansion or vice versa. This is illustrated in Fig. 6.1, which shows examples of possible evolutions of $A(z)$ as function of z for $z_F = 0.05$. Here we take $k = 1.2$ (left frame) and $k = 0.8$ (right). In each case we consider scenarios with $A(z_F) = 1.3$ (slower expansion at T_F than in standard cosmology) as well as $A(z_F) = 0.7$ (faster expansion); moreover, we allow the change of A at $z = z_F$ to be either positive or negative. However, we insist that H remains positive at all times, i.e. $A(z)$ must not cross zero. This excludes scenarios with very large positive $A'(z_{F,\rm st})$, which would lead to $A < 0$ at some $z < z_F$. Similarly, demanding that our ansatz (6.8) remains valid for some range of temperatures above T_F excludes scenarios with very large negative $A'(z_{F,\rm st})$. We will come back to this point shortly.

[1] Presumably the Hubble expansion rate has to approach the standard rate even more closely for $T < T_{\rm BBN}$. However, since all WIMP annihilation effectively ceased well before the onset of BBN, this epoch plays no role in our analysis.

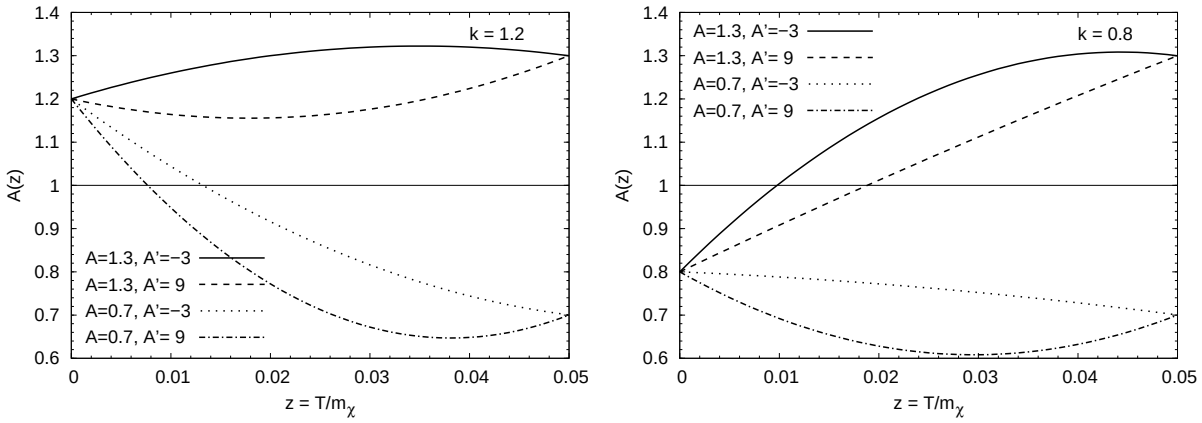

(b)

Figure 6.1: Examples of possible evolutions of the modification parameter $A(z)$ as function of z for $z_F = 0.05$. Here we take $k = 1.2$ (left frame) and $k = 0.8$ (right). In each frame we choose $A(z_F) = 1.3, A'(z_F) = -3$ (thick line), $A(z_F) = 1.3, A'(z_F) = 9$ (dashed), $A(z_F) = 0.7, A'(z_F) = -3$ (dotted), $A(z_F) = 0.7, A'(z_F) = 9$ (dot–dashed).

Eq.(6.7) shows that $z_F \neq z_{F,\rm st}$ ($x_F \neq x_{F,\rm st}$) if $A(z_F) \neq 1$. This is illustrated by Fig. 6.2, which shows the difference between x_F and $x_{F,\rm st}$ in the ($A(z_{F,\rm st})$, $A'(z_{F,\rm st})$) plane. Here we take parameters such that $\Omega_\chi h^2 = 0.099$ in the standard cosmology, which is recovered for $A(z_{F,\rm st}) = 1$, $A'(z_{F,\rm st}) = 0$. Due to the logarithmic dependence on A, x_F (or z_F) differs by at most a few percent from its standard value if $A(z_{F,\rm st})$ is $\mathcal{O}(1)$. Since T_F only depends on the expansion rate at T_F, it is essentially insensitive to the derivative $A'(z_{F,\rm st})$.

In our treatment the modification of the expansion parameter affects the WIMP relic density mostly via the annihilation integral (6.4). In terms of the normalized temperature z, the latter can be rewritten as

$$I(z_F) = \int_0^{z_F} \mathrm{d}z \; G(z)\langle\sigma v\rangle A(z)\,. \tag{6.10}$$

One advantage of the expansion (6.8) is that this integral can be evaluated analytically:

$$\begin{aligned} I(z_F) \;\simeq\; & G(z_F)\left[k(az_F + 3bz_F^2) + (A'(z_{F,\rm st}) - z_{F,\rm st}A''(z_{F,\rm st}))\left(\frac{a}{2}z_F^2 + 2bz_F^3\right)\right. \\ & \left. + \frac{A''(z_{F,\rm st})}{2}\left(\frac{a}{3}z_F^3 + \frac{3b}{2}z_F^4\right)\right]\,. \end{aligned} \tag{6.11}$$

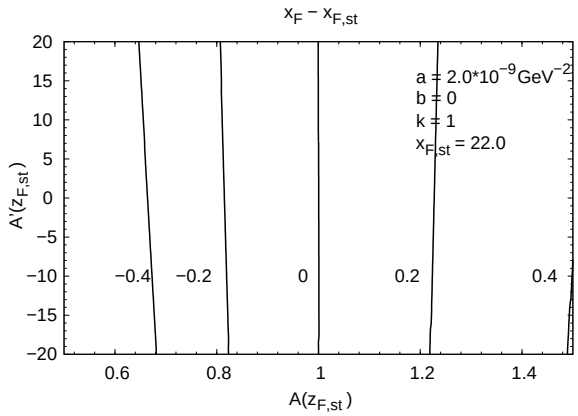

Figure 6.2: Contour plot of $x_F - x_{F,\mathrm{st}}$ in the $(A(z_{F,\mathrm{st}}),\ A'(z_{F,\mathrm{st}}))$ plane. Here we take $a = 2.0 \times 10^{-9}$ GeV^{-2}, $b = 0$, $m_\chi = 100$ GeV, $g_\chi = 2$, $g_* = 90$ (constant) and $k = 1$. This parameter set produces $x_{F,\mathrm{st}} = 22.0$ and $\Omega_\chi h^2 = 0.099$ for the standard approximation.

Here we have assumed that $G(z)$ varies only slowly.

Before proceeding, we first have to convince ourselves that the analytic treatment developed in this Section still works for $A \neq 1$. This is demonstrated by Fig. 6.3, which shows the ratio of the analytic solution obtained from Eqs. (6.5) and (6.11) to the exact one, obtained by numerically integrating the Boltzmann equation (6.2), assuming constant g_*. We see that our analytical treatment is accurate to better than 1%, and can thus safely be employed in the subsequent analysis.

Now we analyze the impact of the modified expansion rate on the WIMP relic density. In Fig. 6.4, we show contour plots of the relic abundance in the $(A(z_{F,\mathrm{st}}),\ A'(z_{F,\mathrm{st}}))$ plane. Recall that large (small) values of A corresponds to a small (large) expansion rate. Since a smaller expansion rate allows the WIMPs more time to annihilate, $A > 1$ leads to a reduced WIMP relic density, whereas $A < 1$ means larger relic density, if the cross section is kept fixed.

However, unlike the freeze–out temperature, the annihilation integral is sensitive to $A(z)$ for all $z \leq z_F$. Note that $A'(z_{F,\mathrm{st}}) > 0$ implies $A(z) < A(z_{F,\mathrm{st}})$ for $z < z_{F,\mathrm{st}} \simeq z_F$. A positive first derivative, $A'(z_{F,\mathrm{st}}) > 0$, can therefore to some extent compensate for

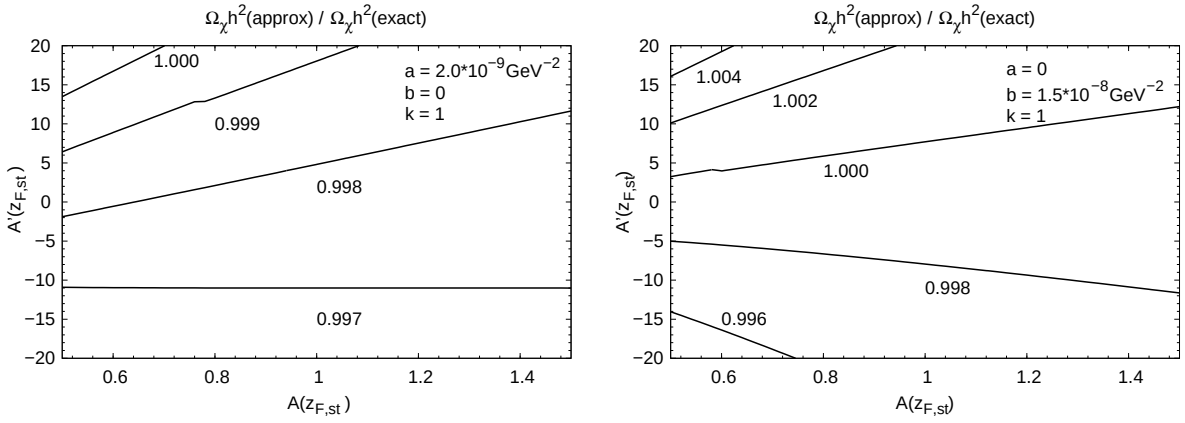

(b)

Figure 6.3: Ratio of the analytic result of the relic density to the exact value in the $(A(z_{F,st}), A'(z_{F,st}))$ plane for $a = 2.0 \times 10^{-9}$ GeV^{-2}, $b = 0$ (left frame) and for $a = 0$, $b = 1.5 \times 10^{-8}$ GeV^{-2} (right). The other parameters are as in Fig. 6.2.

$A(z_{F,\mathrm{st}}) > 1$; analogously, a negative first derivative can compensate for $A(z_{F,\mathrm{st}}) < 1$. This explains the slopes of the curves in Fig. 6.4. Recall also that $A'(z_{F,\mathrm{st}}) = 0$ does not imply a constant modification factor $A(z)$; rather, the term $\propto A''(z_{F,\mathrm{st}})$ in Eq.(6.8) makes sure that A approaches k as $z \to 0$. This explains why a change of A by some given percentage leads to a smaller relative change of $\Omega_\chi h^2$, as can be seen in the Figure. This also illustrates the importance of ensuring appropriate (near–standard) expansion rate in the BBN era. Finally, since the expansion rate at late times is given by H_{st}/k, bigger (smaller) values of k imply that the χ relic density is reduced (enhanced).

6.2 Constraints on the Modification Parameter

Fig. 6.4 shows that we need additional physical constraints if we want to derive bounds on $A(z_{F,\mathrm{st}})$ and/or $A'(z_{F,\mathrm{st}})$. Once the annihilation cross section is known, the requirement (1.1) will single out a region in the space spanned by our three new parameters (including k) which describe the non–standard evolution of the universe, but this region is not bounded. Such additional constraints can be derived from the requirement that the Hubble parameter should remain positive throughout the epoch we are considering. As noted earlier, requiring

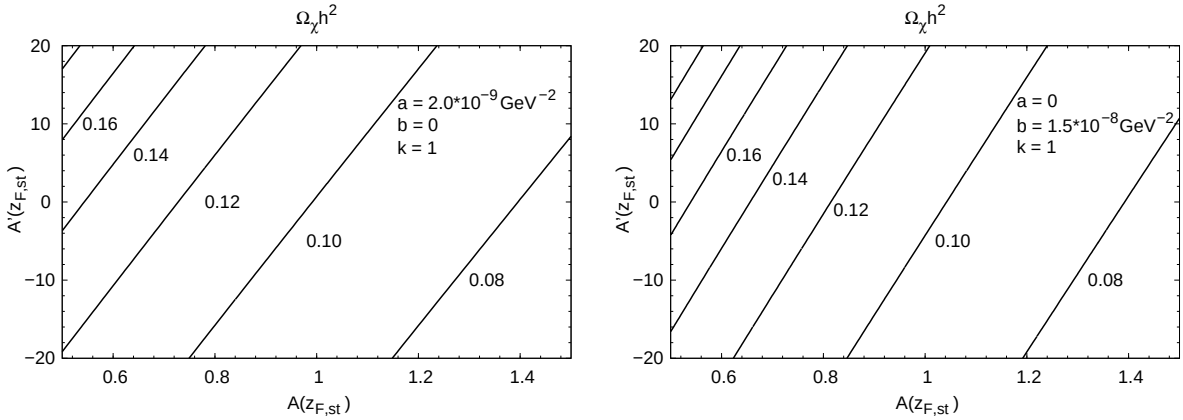

(b)

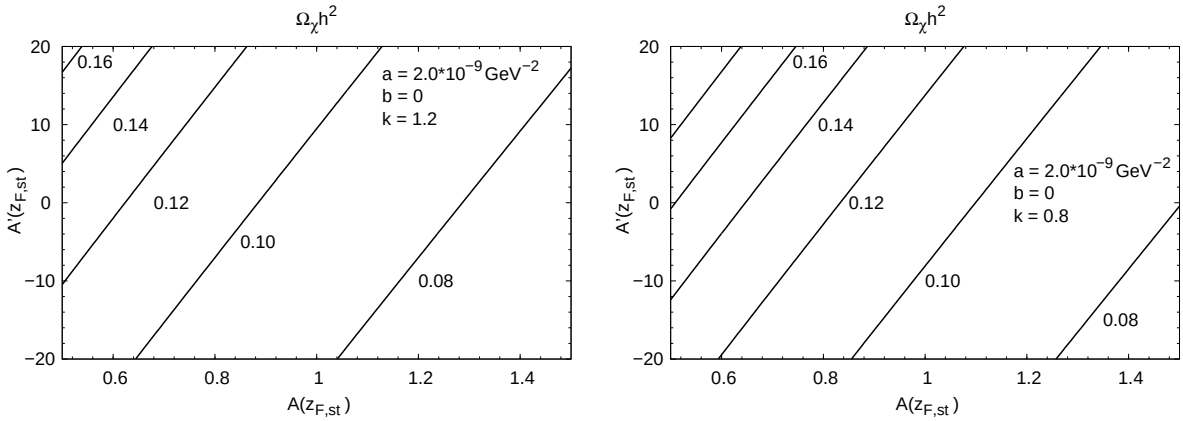

(d)

Figure 6.4: Contour plots of the relic abundance in the $(A(z_{F,st}),\ A'(z_{F,st}))$ plane. Here we choose (a) $a = 2.0 \times 10^{-9}$ GeV^{-2}, $b = 0$, $k = 1$; (b) $a = 0$, $b = 1.5 \times 10^{-8}$ GeV^{-2}, $k = 1$; (c) $a = 2.0 \times 10^{-9}$ GeV^{-2}, $b = 0$, $k = 1.2$; (d) $a = 2.0 \times 10^{-9}$ GeV^{-2}, $b = 0$, $k = 0.8$. The other parameters are as in Fig. 6.2.

$H > 0$ for all $T < T_{F,\mathrm{st}}$ leads to an upper bound on $A'(z_{F,\mathrm{st}})$; explicitly,

$$A'(z_{F,\mathrm{st}}) < \frac{2\left(A(z_{F,\mathrm{st}}) + \sqrt{kA(z_{F,\mathrm{st}})}\right)}{z_{F,\mathrm{st}}}\,. \tag{6.12}$$

On the other hand, a lower bound on $A'(z_{F,\mathrm{st}})$ is obtained from the condition that the modified Hubble parameter is positive between the highest temperature T_i where the ansatz

(6.8) holds and $T_{F,\mathrm{st}}$:

$$A'(z_{F,\mathrm{st}}) > -\left[\frac{1}{z_i - z_{F,\mathrm{st}}}\left(2 - \frac{z_i}{z_{F,\mathrm{st}}}\right) A(z_{F,\mathrm{st}}) + k\left(\frac{1}{z_{F,\mathrm{st}}} - \frac{1}{z_i}\right)\right], \tag{6.13}$$

for $(1 - z_{F,\mathrm{st}}/z_i)^2 k < A(z_{F,\mathrm{st}})$, and

$$A'(z_{F,\mathrm{st}}) > \frac{2\left(A(z_{F,\mathrm{st}}) - \sqrt{kA(z_{F,\mathrm{st}})}\right)}{z_{F,\mathrm{st}}}, \tag{6.14}$$

for $A(z_{F,\mathrm{st}}) < (1 - z_{F,\mathrm{st}}/z_i)^2 k$, where $z_i = T_i/m_\chi$.

Evidently the lower bound on $A'(z_{F,\mathrm{st}})$ depends on z_i, i.e. on the maximal temperature where we assume our ansatz (6.8) to be valid. In ref. [21] we have shown that in standard cosmology ($A \equiv 1$) essentially full thermalization is already achieved for $x_i \lesssim x_F - 0.5$, even if $n_\chi(x_i) = 0$. However, it seems reasonable to demand that H should remain positive at least up to $x_i = x_F -$(a few). In Fig. 6.5 we therefore show the physical constraints on the modification parameter $A(z)$ for $x_{F,\mathrm{st}} - x_i = 4, 10$ and $k = 1$. The dashed and dotted lines correspond to the upper and lower bounds on $A'(z_{F,\mathrm{st}})$, described by Eq.(6.12) and Eqs.(6.13), (6.14), respectively. We see that when $x_{F,\mathrm{st}} - x_i = 4$ the allowed region is $0.4 \lesssim A(z_{F,\mathrm{st}}) \lesssim 6.5$ with $-60 \lesssim A'(z_{F,\mathrm{st}}) \lesssim 400$ for $b = 0$ (left frame), and $0.4 \lesssim A(z_{F,\mathrm{st}}) \lesssim 4.5$ with $-60 \lesssim A'(z_{F,\mathrm{st}}) \lesssim 300$ for $a = 0$ (right frame). When $x_{F,\mathrm{st}} - x_i = 10$, the lower bounds are altered to $0.6 \lesssim A(z_{F,\mathrm{st}})$, $-10 \lesssim A'(z_{F,\mathrm{st}})$ for $b = 0$ (left frame), and $0.6 \lesssim A(z_{F,\mathrm{st}})$, $-20 \lesssim A'(z_{F,\mathrm{st}})$ for $a = 0$ (right frame). Note that the lower bounds on $A(z_{F,\mathrm{st}})$, which depend only weakly on x_i so long as it is not very close to x_F, are almost the same in both cases, which also lead to very similar relic densities in standard cosmology. However, the two upper bounds differ significantly. The reason is that large values of $A(z_{F,\mathrm{st}})$, i.e. a strongly suppressed Hubble expansion, require some degree of finetuning: One also has to take large positive $A'(z_{F,\mathrm{st}})$, so that A becomes smaller than one for some range of z values below z_F, leading to an annihilation integral of similar size as in standard cosmology. Since the $b-$terms show different z_F dependence in the annihilation integral (6.11), the required tuning between $A(z_{F,\mathrm{st}})$ and $A'(z_{F,\mathrm{st}})$ is somewhat different than for the $a-$terms, leading to a steeper slope of the allowed region. This allowed region therefore saturates the upper bound (6.12) on the slope for somewhat smaller $A(z_{F,\mathrm{st}})$.

The effect of this tuning can be seen by analyzing the special case where $A''(z_{F,\mathrm{st}}) = 0$.

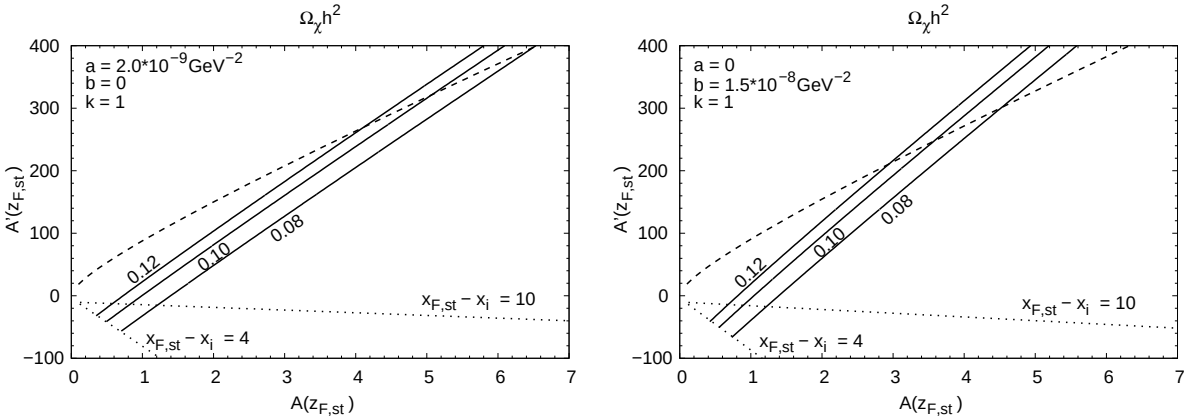

(b)

Figure 6.5: Contour plots of the relic abundance $\Omega_\chi h^2$ in the $(A(z_{F,\rm st}), A'(z_{F,\rm st}))$ planes. The dashed line corresponds to the upper bound on $A'(z_{F,\rm st})$. The dotted lines correspond to the lower bounds calculated for $x_{F,\rm st} - x_i = 4, 10$. We take $a = 2.0 \times 10^{-9}$ GeV^{-2}, $b = 0$ (left frame) and $a = 0$, $b = 1.5 \times 10^{-8}$ GeV^{-2} (right frame). The other parameters are as in Fig 6.2.

The modification parameter then reads

$$A(z) = \frac{A(z_{F,\rm st}) - k}{z_{F,\rm st}} z + k \,. \tag{6.15}$$

Note that A is now a monotonic function of z, making large cancellations in the annihilation integral impossible. Imposing that $A(z)$ remains positive for $z_{F,\rm st} \leq z \leq z_i$ leads to the lower limit

$$A(z_{F,\rm st}) > \left(1 - \frac{z_{F,\rm st}}{z_i}\right) k \,. \tag{6.16}$$

There is no upper bound, since $A(z)$ is now automatically positive for all $z \in [0, z_{F,\rm st}]$ if $A(z_{F,\rm st})$ and $A(0) \equiv k$ are both positive. Fig. 6.6 shows constraints on the relic abundance in the $(A(z_{F,\rm st}), k)$ plane for $A''(z_{F,\rm st}) = 0$. The dotted lines correspond to the lower bounds (6.16) on $A(z_{F,\rm st})$ for $x_{F,\rm st} - x_i = 4, 10$. As noted earlier, k is constrained by the BBN bound. This leads to the bounds $0.5 \lesssim A(z_{F,\rm st}) \lesssim 1.8$ for $b = 0$ (left frame), and $0.65 \lesssim A(z_{F,\rm st}) \lesssim 1.6$ for $a = 0$ (right frame), when $x_{F,\rm st} - x_i = 10$. Evidently the constraints now only depend weakly on whether the $a-$ or $b-$term dominates in the annihilation cross section. As the initial temperature is lowered, the impact of the constraint (6.16) disappears.

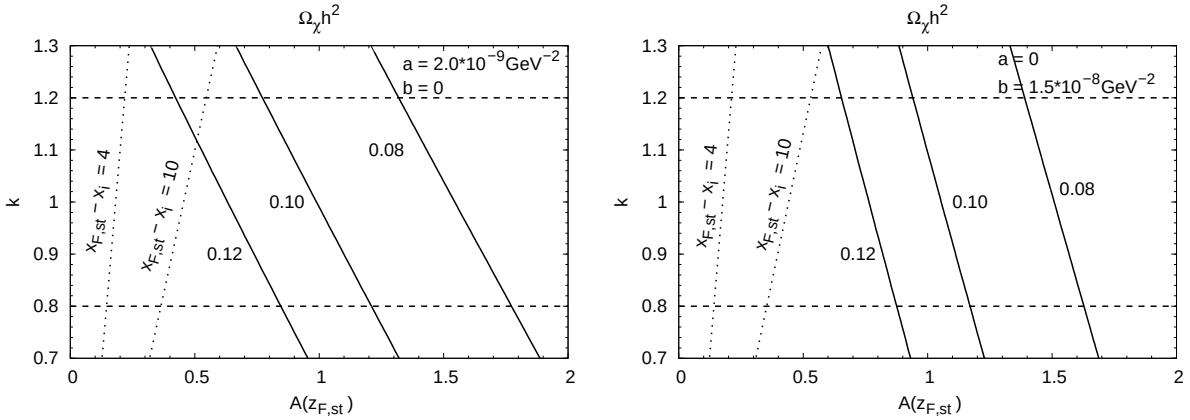

(b)

Figure 6.6: Contour plots of the relic abundance $\Omega_\chi h^2$ in the $(A(z_{F,\mathrm{st}}), k)$ plane for $A''(z_{F,\mathrm{st}}) = 0$. The dotted lines correspond to the lower bounds of $A(z_{F,\mathrm{st}})$, calculated for $x_{F,\mathrm{st}} - x_i = 4, 10$. We take $a = 2.0 \times 10^{-9}$ GeV^{-2}, $b = 0$ (left frame) and $a = 0$, $b = 1.5 \times 10^{-8}$ GeV^{-2} (right frame). The other parameters are as in Fig 6.2.

So far we have assumed in this Section that the reheat temperature was high enough for WIMPs to have attained full thermal equilibrium. If this was not the case, the initial temperature as well as the suppression parameter affects the final relic abundance. Here we show that the lower bound on the reheat temperature derived in the previous Section survives even in scenarios with altered expansion history as long as WIMPs were only produced thermally.

This can be understood from the observation that the Boltzmann equation with modified expansion rate is obtained by replacing $\langle\sigma v\rangle$ in the radiation–dominated case by $\langle\sigma v\rangle A$. Increasing (decreasing) A therefore has the same effect as an increase (decrease) of the annihilation cross section. Since the lower bound on T_0 was independent of σ (more exactly: we quoted the absolute minimum, for the optimal choice of σ), we expect it to survive even if $A(z) \neq 1$ is introduced.

This is borne out by Fig. 6.7, which shows the relic abundance $\Omega_\chi h^2$ in the $(A(z_{F,st}), x_0)$ plane for the simplified case $A''(z_{F,\mathrm{st}}) = 0$; similar results can be obtained for the more

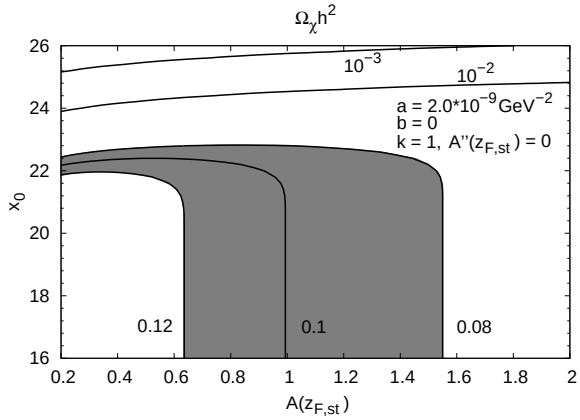

Figure 6.7: Contour plot of the relic abundance $\Omega_\chi h^2$ in the $(A(z_{F,st}),\ x_0)$ plane. Here we choose $a = 2.0 \times 10^{-9}$ GeV^{-2}, $b = 0$, $k = 1, A''(z_{F,\mathrm{st}}) = 0$. The other parameters are as in Fig. 6.2. The shaded region corresponds to the WMAP bound on the cold dark matter abundance, $0.08 < \Omega_{\mathrm{CDM}} h^2 < 0.12$ (95% C.L.).

general ansatz (6.8). The shaded region corresponds to the bound (1.1) on the cold dark matter abundance. As expected, this figure looks similar to Fig. 4.7 if the annihilation cross section in Fig. 4.7 is replaced by $A(z_{F,\mathrm{st}})$. The maximal value of x_0 consistent with the WMAP data remains around 23 even in these scenarios with modified expansion rate. Fig. 6.7 also shows that $A(z_{F,\mathrm{st}}) \ll 1$ is allowed for some narrow range of initial temperature $T_0 < T_F$. This is analogous to the low cross section branch in Fig. 4.7.

Chapter 7

Conclusions and Discussion

In this thesis, we studied the relic density of non–relativistic long–lived or stable particles χ in non–standard cosmological scenarios with special emphasis on low–temperature scenarios and the scenario where the pre–BBN Hubble parameter is modified using both analytical and numerical methods.

In the low–temperature scenario, we assumed particles never reach thermal equilibrium because of the low reheat temperature after the end of inflation. Such scenarios are interesting because they lower the predicted relic abundance and therefore open the parameter space of particle physics models, allowing combinations of parameters which are cosmologically disfavored in the standard high temperature scenario.

In the case of small χ annihilation cross section or very low temperature, the annihilation term in the Boltzmann equation (4.1) is negligible, leading to the zeroth order solution Y_0 of Eq.(4.4). We add δ as in Eq.(4.8) to describe the effect of annihilation of particles when both the annihilation and production play a crucial role in determining the relic abundance while thermal equilibrium is not fully achieved. Unfortunately this approximation breaks down well before χ attains full thermal equilibrium. On the other hand, we found the "re–summed" ansatz Eq.(4.15), which is obtained by resumming the annihilation term δ in Eq.(4.8), and pointed out the solution describes the full temperature dependence of the χ number density as long as χ does not reach full equilibrium. It works even if a non–thermal source of χ production is added. For higher cross sections or temperatures even the re–summed ansatz fails to describe the temperature dependence of the χ number density at intermediate temperatures. However, by replacing the initial scaled inverse temperature x_0 with the quantity $x_{0,\max}$ of Eq.(4.22) our ansatz succeeds in predicting the final relic

density about as well as the standard semi–analytical high temperature treatment does, with comparable numerical effort.

From the particle physics point of view, the main effect of a low reheat temperature is that it allows to reproduce the correct relic density in scenarios with low annihilation cross section, e.g. for bino–like neutralinos and large sfermion masses. Conversely, the non–thermal production mechanism studied in Chapter 4 allows to reproduce the correct relic density for WIMPs with large annihilation cross section, e.g. wino–like neutralinos [30]. As noticed in [20], the combination of these effects in principle allows to completely decouple the WIMP relic density from its annihilation cross section. In many studies of expected WIMP detection rates scenarios yielding too high a relic density under the standard assumptions were not considered; such scenarios typically also lead to low detection rates. Conversely, in scenarios leading to too low a thermal WIMP density, which typically predict large detection rates for fixed WIMP density, the predicted detection rates were often rescaled by the ratio of the predicted to the observed relic density. If one allows lower reheat temperatures and/or non–thermal WIMP sources, the possible range of signals for WIMP detection can therefore be enlarged towards both larger and smaller values.

On the other hand, by applying the observed cosmological amount of cold dark matter to the predicted WIMP abundance, we obtain the lower bound of the initial temperature T_0 of the radiation–dominated period after inflation. In terms of the normalized inverse temperature the bound is shown to be $x_0 \equiv m_\chi/T_0 \lesssim 23$.

We also investigated the effect of non–standard expansion rate of the universe on the WIMP relic abundance. In general the abundance of thermal relics depends on the ratio of the annihilation cross section to the expansion rate; the latter is determined in standard cosmology. We found that even for non–standard Hubble parameter the relic abundance calculated accurately in terms of an annihilation integral, very similar to the case of standard cosmology. We assumed that the WIMP annihilation cross section is such that the standard scenario yields the observed relic density, and parameterized the modification of the Hubble parameter as a quadratic function of the temperature. At low temperatures the Hubble parameter approaches its standard value to within $\sim 20\%$ in order not to conflict with the successful prediction of BBN.

Of course in order to draw the conclusions derived in this thesis, we need to convince ourselves that WIMPs do indeed form (nearly) all DM. This requires not only the detec-

tion of WIMPs, e.g. in direct search experiments; we also need to show that their density is in accord with the local Dark Matter density derived from astronomical observations. To that end, the cross sections appearing in the calculation of the detection rate need to be known independently. This can only be done in the framework of a definite theory, using data from collider experiments. For example, in order to determine the cross section for the direct detection of supersymmetric WIMPs, one needs to know the parameters of the supersymmetric neutralino, Higgs and squark sectors [3]. We also saw that inferences about $H(T_F)$ can only be made if the WIMP annihilation cross section is known. This again requires highly non–trivial analyses of collider data [88], as well as a consistent overall theory. We thus see that the interplay of accurate cosmological data with results obtained from dark matter detections and collider experiments can give us insight into the pre–BBN universe, which to date remains unexplored territory.

Acknowledgments

I would like to thank my Professor Manuel Drees for his support and instruction to my work during my Phd. In these 3 years of my Phd studying, he is always ready to discuss problems which I faced in my work. He is kind not only in my work, but also in my personal life in Bonn. He introduced me to the field of astroparticle physics.

I would like to thank my collaborator Mitsuru Kakizaki for his collaboration on these work and I deeply appreciate his limitless help for understanding physics and computer language problems during my Phd work. I also thanks to him for correcting my thesis in detail.

I would like to thank Andreas Wisskirchen for his various help in these 3 years. I would like to thank the secretaries D. Fabender, S. Heidbrink and P. Zündorf for their kind help in these 3 years.

Finally I thank my husband Kayser Musa from deep of my heart for his unconditional support for my studying.

Appendix A

Exponential Functions

In this appendix, we give explicit expressions for the functions $F_n^m(x, x_0)$, $G_n^r(x, x_0)$, $G_n^{r/2}(x, x_0)$ and $G_n^c(x, x_0)$ which appear in Chapters 4 and 5. These functions are analytically expressed in terms of the exponential integral of the first order $\mathrm{E}_1(x)$ and the error function $\mathrm{erfc}(x)$.

First we review the exponential integral and the error function. The exponential integral of the first order is defined by

$$\mathrm{E}_1(x) = \int_1^\infty dt\ \frac{\mathrm{e}^{-xt}}{t} = \int_x^\infty dt\ \frac{\mathrm{e}^{-t}}{t}\,. \tag{A.1}$$

We need this function only for $x > x_0 \gg 1$. We can then use the asymptotic large x expansion,

$$\mathrm{E}_1(x) \sim \frac{\mathrm{e}^{-x}}{x} \sum_{n=0}^{\infty} \frac{(-1)^n n!}{x^n}\,. \tag{A.2}$$

The error function is defined by

$$\mathrm{erfc}(x) \;=\; \frac{2}{\sqrt{\pi}} \int_x^\infty dt\ \mathrm{e}^{-t^2}\,, \tag{A.3}$$

with asymptotic large x expansion

$$\mathrm{erfc}(x) \sim \frac{\mathrm{e}^{-x^2}}{\sqrt{\pi}x} \sum_{n=0}^{\infty} \frac{(-1)^n (2n-1)!!}{(2x^2)^n}\,. \tag{A.4}$$

The functions $F_n^m(x, x_0)$ are defined by

$$F_n^m(x, x_0) = \int_{x_0}^x dt\ \frac{\mathrm{e}^{-mt}}{t^n}\,. \tag{A.5}$$

These integrals can be reduced to the form (A.1). The resulting expressions and corresponding asymptotic expansions, computed from Eq.(A.2), are:

$$
\begin{aligned}
F_0^4(x,x_0) &= \frac{1}{4}(\mathrm{e}^{-4x_0}-\mathrm{e}^{-4x})\,,\\
F_1^4(x,x_0) &= \mathrm{E}_1(4x_0)-\mathrm{E}_1(4x)\\
&\sim \frac{\mathrm{e}^{-4x_0}}{4x_0}\left(1-\frac{1}{4x_0}\right)-\frac{\mathrm{e}^{-4x}}{4x}\left(1-\frac{1}{4x}\right)+\mathcal{O}\left(\frac{\mathrm{e}^{-4x_0}}{x_0^3}\right),\\
F_2^4(x,x_0) &= \frac{\mathrm{e}^{-4x_0}}{x_0}-4\mathrm{E}_1(4x_0)-\frac{\mathrm{e}^{-4x}}{x}+4\mathrm{E}_1(4x)\\
&\sim \frac{\mathrm{e}^{-4x_0}}{4x_0^2}-\frac{\mathrm{e}^{-4x}}{4x^2}+\mathcal{O}\left(\frac{\mathrm{e}^{-4x_0}}{x_0^3}\right),\\
F_3^4(x,x_0) &= \frac{\mathrm{e}^{-4x_0}}{2x_0^2}-2\frac{\mathrm{e}^{-4x_0}}{x_0}+8E_1(4x_0)-\frac{\mathrm{e}^{-4x}}{2x^2}+2\frac{\mathrm{e}^{-4x}}{x}-8E_1(4x)\\
&\sim \mathcal{O}\left(\frac{\mathrm{e}^{-4x_0}}{x_0^3}\right),\\
F_1^2(x,x_0) &= \mathrm{E}_1(2x_0)-\mathrm{E}_1(2x)\\
&\sim \frac{\mathrm{e}^{-2x_0}}{2x_0}\left(1-\frac{1}{2x_0}\right)-\frac{\mathrm{e}^{-2x}}{2x}\left(1-\frac{1}{2x}\right)+\mathcal{O}\left(\frac{\mathrm{e}^{-2x_0}}{x_0^3}\right),\\
F_2^2(x,x_0) &= \frac{\mathrm{e}^{-2x_0}}{x_0}-2\mathrm{E}_1(2x_0)-\frac{\mathrm{e}^{-2x}}{x}+2\mathrm{E}_1(2x)\\
&\sim \frac{\mathrm{e}^{-2x_0}}{2x_0^2}-\frac{\mathrm{e}^{-2x}}{2x^2}+\mathcal{O}\left(\frac{\mathrm{e}^{-2x_0}}{x_0^3}\right),\\
F_3^2(x,x_0) &= \frac{\mathrm{e}^{-2x_0}}{2x_0^2}-\frac{\mathrm{e}^{-2x_0}}{x_0}+2E_1(2x_0)-\frac{\mathrm{e}^{-2x}}{2x^2}+\frac{\mathrm{e}^{-2x}}{x}-2E_1(2x)\\
&\sim \mathcal{O}\left(\frac{\mathrm{e}^{-2x_0}}{x_0^3}\right),\\
F_2^0(x,x_0) &= \frac{1}{x_0}-\frac{1}{x}\,,\\
F_3^0(x,x_0) &= \frac{1}{2x_0^2}-\frac{1}{2x^2}\,.
\end{aligned}
\tag{A.6}
$$

The functions $G_n^r(x,x_0)$ and $G_n^{r/2}(x,x_0)$ are defined by

$$
\begin{aligned}
G_n^r(x,x_0) &= \int_{x_0}^{x} dt\,\frac{\mathrm{e}^{-rt^2}}{t^n}\,,\\
G_n^{r/2}(x,x_0) &= \int_{x_0}^{x} dt\,\frac{\mathrm{e}^{-rt^2/2}}{t^n}\,,\quad n=2,3\,.
\end{aligned}
\tag{A.7}
$$

Using Eqs.(A.3) and (A.4), we find the following explicit expressions and corresponding

asymptotic expansions:

$$
\begin{aligned}
G_2^r(x,x_0) &= \frac{\mathrm{e}^{-rx_0^2}}{x_0} - \sqrt{\pi r}\ \mathrm{erfc}(\sqrt{r}x_0) - \frac{\mathrm{e}^{-rx^2}}{x} + \sqrt{\pi r}\ \mathrm{erfc}(\sqrt{r}x) \\
&\sim \frac{\mathrm{e}^{-rx_0^2}}{2rx_0^3}\left(1-\frac{3}{2rx_0^2}\right) - \frac{\mathrm{e}^{-rx^2}}{2rx^3}\left(1-\frac{3}{2rx^2}\right) + \mathcal{O}\left(\frac{\mathrm{e}^{-rx_0^2}}{x_0(rx_0^2)^3}\right), \\
G_3^r(x,x_0) &= \frac{\mathrm{e}^{-rx_0^2}}{2x_0^2} - \frac{r}{2}\ \mathrm{E}_1(rx_0^2) - \frac{\mathrm{e}^{-rx^2}}{2x^2} + \frac{r}{2}\ \mathrm{E}_1(rx^2) \\
&\sim \frac{\mathrm{e}^{-rx_0^2}}{2rx_0^4}\left(1-\frac{2}{rx_0^2}\right) - \frac{\mathrm{e}^{-rx^2}}{2rx^4}\left(1-\frac{2}{rx^2}\right) + \mathcal{O}\left(\frac{\mathrm{e}^{-rx_0^2}}{x_0^2(rx_0^2)^3}\right), \\
G_2^{r/2}(x,x_0) &= \frac{\mathrm{e}^{-rx_0^2/2}}{x_0} - \sqrt{\frac{\pi r}{2}}\ \mathrm{erfc}\left(\sqrt{\frac{r}{2}}x_0\right) - \frac{\mathrm{e}^{-rx^2/2}}{x} + \sqrt{\frac{\pi r}{2}}\ \mathrm{erfc}\left(\sqrt{\frac{r}{2}}x\right) \\
&\sim \frac{\mathrm{e}^{-rx_0^2/2}}{rx_0^3}\left(1-\frac{3}{rx_0^2}\right) - \frac{\mathrm{e}^{-rx^2/2}}{rx^3}\left(1-\frac{3}{rx^2}\right) + \mathcal{O}\left(\frac{\mathrm{e}^{-rx_0^2}}{x_0(rx_0^2)^3}\right), \\
G_3^{r/2}(x,x_0) &= \frac{\mathrm{e}^{-rx_0^2/2}}{2x_0^2} - \frac{r}{4}\ \mathrm{E}_1\left(\frac{rx_0^2}{2}\right) - \frac{\mathrm{e}^{-rx^2/2}}{2x^2} + \frac{r}{4}\ \mathrm{E}_1\left(\frac{rx^2}{2}\right) \\
&\sim \frac{\mathrm{e}^{-rx_0^2/2}}{rx_0^4}\left(1-\frac{4}{rx_0^2}\right) - \frac{\mathrm{e}^{-rx^2/2}}{rx^4}\left(1-\frac{4}{rx^2}\right) + \mathcal{O}\left(\frac{\mathrm{e}^{-rx_0^2}}{x_0^2(rx_0^2)^3}\right). \qquad \text{(A.8)}
\end{aligned}
$$

In the expansion we assume that $rx_0^2 \sim x_0$, so that the effect of non–thermal χ production is comparable to that of thermal production.

Finally, the functions $G_n^c(x,x_0)$ are defined by

$$
G_n^c(x,x_0) = \int_{x_0}^{x} dt\ \frac{\mathrm{e}^{-2t-rt^2/2}}{t^n}, \quad n=1,2,3\,. \qquad \text{(A.9)}
$$

They appear in the "interference terms" in Eq.(5.6), which are important only if thermal and non–thermal contributions to Y_0 in Eq.(5.4) are comparable in size. Since the overall $t-$dependence of the integrand in Eq.(A.9) is dominated by the numerator, we can, to good approximation, evaluate these functions by replacing t in the denominator by some

appropriate constant x_c:

$$\begin{aligned} G_n^c(x,x_0) &\simeq \int_{x_0}^{x} dt\ \frac{\mathrm{e}^{-2t-rt^2/2}}{x_c^n} \\ &= \frac{\mathrm{e}^{2/r}}{x_c^n}\sqrt{\frac{\pi}{2r}}\left[\mathrm{erfc}\left(\frac{1}{\sqrt{2r}}(rx_0+2)\right)-\mathrm{erfc}\left(\frac{1}{\sqrt{2r}}(rx+2)\right)\right] \\ &\sim \frac{\mathrm{e}^{-2x_0-rx_0^2/2}}{x_c^n(rx_0+2)}\left[1-\frac{r}{(rx_0+2)^2}\right]-\frac{\mathrm{e}^{-2x-rx^2/2}}{x_c^n(rx+2)}\left[1-\frac{r}{(rx+2)^2}\right] \\ &\quad +\mathcal{O}\left(\frac{\mathrm{e}^{-2x_0-rx_0^2/2}}{x_0^{n-1}(rx_0^2)^3}\right)\ . \end{aligned} \tag{A.10}$$

In our calculations in Chapter 5 we set $x_c = x_0$; this over–estimates G_n^c by a few %, with negligible error in $Y_{1,r}$.

Bibliography

[1] WMAP Collab., D. N. Spergel *et al.*, "First Year Wilkinson Microwave Anisotropy Probe (WMAP) Observations: Determination of Cosmological Parameters," Astrophys. J. Suppl. **148**, 175 (2003) [arXiv:astro–ph/0302209]; "Wilkinson Microwave Anisotropy Probe (WMAP) Three Year Results: Implications for Cosmology," [arXiv:astro–ph/0603449].

[2] E. W. Kolb and M. S. Turner, "The Early Universe," Addison–Wesley (Redwood City, CA, 1990).

[3] For a review see G. Jungman, M. Kamionkowski, K. Griest, "Supersymmetric Dark Matter," Physics Reports **267**, 195–373 (1996); G. Bertone, D. Hooper and J. Silk, "Particle Dark Matter: Evidence, Candidates and Constraints," Phys. Rep. **405**, 279 (2005) [arXiv:hep–ph/0404175].

[4] M. Drees, M. Nojiri, "Neutralino relic density in minimal N=1 supergravity," Phys. Rev. D **47**, 376 – 408 (1993)

[5] M. Drees, M. M. Nojiri, D. P. Roy and Y. Yamada, "Light Higgsino dark matter," Phys. Rev. D **56**, 276 (1997) [Erratum–ibid. D **64**, 039901 (2001)] [arXiv:hep–ph/9701219].

[6] K. Griest and D. Seckel, "Three exceptions in the calculation of relic abundances," Phys. Rev. D **43**, 3191 (1991).

[7] G. Servant and T. M. P. Tait, "Is the lightest Kaluza–Klein particle a viable dark matter candidate?," Nucl. Phys. B **650**, 391 (2003) [arXiv:hep–ph/0206071].

[8] D. Hooper and S. Profumo, "Dark matter and collider phenomenology of universal extra dimensions," [arXiv:arXiv:hep–ph/0701197].

[9] A. Birkedal–Hansen and J. G. Wacker, "Scalar dark matter from theory space," Phys. Rev. D **69**, 065022 (2004) [arXiv:hep–ph/0306161].

[10] J. Hubisz and P. Meade, "Phenomenology of the littlest Higgs with T–parity," Phys. Rev. D **71**, 035016 (2005) [arXiv:hep–ph/0411264].

[11] A. Martin, "Dark matter in the simplest little Higgs model," [arXiv:hep–ph/0602206].

[12] J. R. Ellis, K. A. Olive, Y. Santoso and V. C. Spanos, "Supersymmetric dark matter in light of WMAP," Phys. Lett. B **565**, 176 (2003) [arXiv:hep–ph/0303043].

[13] L. J. Rosenberg and K. A. van Bibber, "Searches for Invisible Axions," Phys. Rept. **325**, 1 (2000).

[14] R. J. Scherrer and M. S. Turner, Phys. Rev. D **33**, 1585 (1986), "On The Relic, Cosmic Abundance Of Stable Weakly Interacting Massive Particles," [Erratum–ibid. D **34**, 3263 (1986)].

[15] For a review, see e.g. D. H. Lyth and A. Riotto, "Particle Physics Models of Inflation and the Cosmological Density Perturbation," Phys. Rep. **314**, 1 (1999) [arXiv:hep–ph/9807278].

[16] G. F. Giudice, E. W. Kolb and A. Riotto, "Largest temperature of the radiation era and its cosmological implications," Phys. Rev. D **64**, 023508 (2001) [arXiv:hep–ph/0005123].

[17] M. Kawasaki, K. Kohri and N. Sugiyama, "Cosmological Constraints on Late–time Entropy Production," Phys. Rev. Lett. **82**, 4168 (1999) [arXiv:astro–ph/9811437]; " MeV–scale Reheating Temperature and Thermalization of Neutrino Background," Phys. Rev. D **62**, 023506 (2000) [arXiv:astro–ph/0002127]; S. Hannestad, "What is the lowest possible reheating temperature?," Phys. Rev. D **70**, 043506 (2004) [arXiv:astro–ph/0403291]; K. Ichikawa, M. Kawasaki and F. Takahashi, "The oscillation effects on thermalization of the neutrinos in the universe with low reheating temperature," Phys. Rev. D **72**, 043522 (2005) [arXiv:astro–ph/0505395].

[18] N. Fornengo, A. Riotto and S. Scopel, "Supersymmetric Dark Matter and the Reheating Temperature of the Universe," Phys. Rev. D **67**, 023514 (2003) [arXiv:hep–ph/0208072].

[19] M. Bastero–Gil and S. F. King, "Leptogenesis in a Realistic Supersymmetric Model of Inflation with a Low Reheat Temperature," Phys. Rev. D **63** 123509 (2001) [arXiv:hep–ph/0011385]; A. Kudo and M. Yamaguchi, "Inflation with Low Reheat Temperature and Cosmological Constraint on Stable Charged Massive Particles," Phys. Lett. B **516**, 151 (2001) [arXiv:hep–ph/0103272].

[20] G. Gelmini and P. Gondolo, "Neutralino with the Right Cold Dark Matter Abundance in (Almost) Any Supersymmetric Model," Phys. Rev. D **74**, 023510 (2006) [arXiv:hep–ph/0602230]; G. Gelmini, P. Gondolo, A. Soldatenko and C. E. Yaguna, "The effect of a late decaying scalar on the neutralino relic density," Phys. Rev. D **74**, 083514 (2006) [arXiv:hep–ph/0605016].

[21] M. Drees, H. Iminniyaz and M. Kakizaki, "Abundance of Cosmological Relics in Low–Temperature Scenarios," Phys. Rev. D **73**, 123502 (2006) [arXiv:hep–ph/0603165].

[22] D. J. H. Chung, E. W. Kolb and A. Riotto, "Production of massive particles during reheating," Phys. Rev. D **60**, 063504 (1999) [arXiv:hep–ph/9809453].

[23] R. Allahverdi and M. Drees, "Thermalization after inflation and production of massive stable particles," Phys. Rev. D **66**, 063513 (2002) [arXiv:hep–ph/0205246].

[24] C. Pallis, "Massive Particle Decay and Cold Dark Matter Abundance," Astropart. Phys. **21**, 689 (2004) [arXiv:hep–ph/0402033].

[25] J. H. Traschen and R. H. Brandenberger, "Particle production during out–of–equilibrium phase transitions," Phys. Rev. D **42**, 2491 (1990); L. Kofman, A. D. Linde and A. A. Starobinsky, "Reheating after Inflation", Phys. Rev. Lett. **73**, 3195 (1994) [arXiv:hep–th/9405187] and "Towards the Theory of Reheating After Inflation," Phys. Rev. D **56**, 3258 (1997) [arXiv:hep–ph/9704452].

[26] R. Allahverdi and M. Drees, "Production of massive stable particles in inflaton decay," Phys. Rev. Lett. **89**, 091302 (2002) [arXiv:hep–ph/0203118].

[27] R. Allahverdi and A. Mazumdar, "Quasi–thermal Universe and its implications for gravitino production, baryogenesis and dark matter," [arXiv:hep–ph/0505050] ; " Supersymmetric thermalization and quasi–thermal universe: consequences for gravitinos and leptogenesis," [arXiv:hep–ph/0512227].

[28] R. J. Scherrer and M. S. Turner, "The shadow world of superstring theories," Phys. Rev. D **31**, 681 (1985); G. Lazarides, R. K. Schaefer, D. Seckel and Q. Shafi, "Dilution of cosmological axions by entropy production," Nucl. Phys. B **346**, 193 (1990); J. E. Kim, "Effects of decay of the scalar partner of the axion on cosmological bounds on axion supermultiplet properties," Phys. Rev. Lett. **67**, 3465 (1991).

[29] M. Kamionkowski and M. S. Turner, "Thermal relics: Do we know their abundances?," Phys. ReV. D **42**, 3310 (1990).

[30] T. Moroi and L. Randall, "Wino Cold Dark Matter from Anomaly–Mediated SUSY Breaking," Nucl. Phys. B **570**, 455 (2000) [arXiv:hep–ph/9906527].

[31] M. Endo and F. Takahashi, "Non–thermal production of dark matter from late–decaying scalar field at intermediate scale," Phys. Rev. D **74**, 063502 (2006) [arXiv:hep–ph/0606075].

[32] R. Catena, N. Fornengo, A. Masiero, M. Pietroni and F. Rosati, "Dark Matter Relic Abundance and Scalar–Tensor Dark Energy," Phys. Rev. D **70**, 063519 (2004) [arXiv:astro–ph/0403614].

[33] P. Salati, "Quintessence and the Relic Density of Neutralinos," Phys. Lett. B **571**, 121 (2003) [arXiv:astro–ph/0207396].

[34] N. Okada and O. Seto, "Relic density of dark matter in brane world cosmology," Phys. Rev. D **70**, 083531 (2004) [arXiv:hep–ph/0407092].

[35] A. B. Lahanas, N. E. Mavromatos and D. V. Nanopoulos, "Smoothly evolving Supercritical–String Dark Energy relaxes Supersymmetric–Dark–Matter Constraints," [arXiv:hep–ph/0612152].

[36] M. Drees, H. Iminniyaz and M. Kakizaki, "Constraints on the very early universe from WIMP dark matter," arXiv:0704.1590 [hep–ph].

[37] F. Zwicky, "Spectral displacement of extra galactic nebulae," Helv. Phys. Acta **6**, 110, 1933.

[38] J. K. Adelman-McCarthy *et al.* [SDSS Collaboration], "The Fourth Data Release of the Sloan Digital Sky Survey," Astrophys. J. Suppl. **162**, 38 (2006) [arXiv:astro–ph/0507711].

[39] S. Cole *et al.* [The 2dFGRS Collaboration], "The 2dF Galaxy Redshift Survey: Power–spectrum analysis of the final dataset and cosmological implications," Mon. Not. Roy. Astron. Soc. **362**, 505 (2005) [arXiv:astro–ph/0501174].

[40] K. G. . Begeman, A. H. Broeils and R. H. Sanders, "Extended rotation curves of spiral galaxies–dark haloes and modified dynamics," MNRAS, **249**, 523 (1991).

[41] A. Slyz, T. Kranz and H. W. Rix, "Exploring spiral galaxy potentials with hydrodynamical simulations," Mon. Not. Roy. Antron. Soc. **346**, 1162 (2003) [arXiv:astro–ph/0309597].

[42] J. A. Tyson and P. Fischer, "Measurement of the Mass Profile of Abell 1689," Astrophys, J. Lett. **446**, L55 (1995).

[43] N. Bahcall and X. Fan, "The Most Massive Distant Clusters: Determining W, and s8" Astrophys. J. **504**, 1 (1998).

[44] A. Kashlinsky, "Determining Ω from cluster correlation function," Phys. Rept. **307**, 67 (1998) [arXiv:astro–ph/9806236].

[45] R. G. Carlberg, *et al.*, "The $\Omega_M - \Omega_\lambda$ Dependence of the Apparent Cluster Ω," Astrophys. J. **516**, 552 (1999).

[46] D. J. Eisenstein *et al.* [SDSS Collaboration], "Detection of the Baryon Acoustic Peak in the Large–Scale Correlation Function of SDSS Luminous Red Galaxies," Astrophys. J. **633**, 560 (2005) [arXiv:astro–ph/0501171].

[47] C. L. Bennett, *et al.* 2003a, "First–Year Wilkinson Microwave Anisotropy Probe (WMAP) Observations: Preliminary Maps and Basic Results," Astrophys. J. Suppl. **148**, 1 (2003) [arXiv:astro–ph/0302207]; C. L. Bennett, *et al.* 2003b, "First Year Wilkinson Microwave Anisotropy Probe (WMAP) Observations: Foreground Emission," Astrophys. J. Suppl. **148**, 97 (2003) [arXiv:astro–ph/0302208].

[48] Hinshaw *et al.* 2003b "First–Year Wilkinson Microwave Anisotropy Probe (WMAP) Observations: The Angular Power Spectrum," Astrophys. J. Suppl. **148**, 135 (2003).

[49] K. A. Olive, "TASI Lectures on dark matter," [arXiv:astro–ph/0301505].

[50] W. M. Yao *et al.* [Particle Data Group], "Review of Particle Physics," J. Phys. G. **33**, 224 (2006).

[51] http://map.gsfc.nasa.gov/.

[52] MACHO collab., C. Alcock *et al.* "Possible gravitational microlensing of a star in the Large Magellanic Cloud," Nature **365**, 621 (1993); EROS collab., E. Aubourg *et al.*, "Astronomy–Gravitational microlens in motion," Nature **365**, 623 (1993); W. Sutherland *et al.* "Gravitational microlensing results from MACHO," [arXiv:astro–ph/9611059].

[53] L. Bergstrom, "Non–Baryonic Dark Matter – Observational Evidence and Detection Methods," Rept. Prog. Phys. **63**, 793 (2000) [arXiv:hep–ph/0002126].

[54] W. M. Yao *et al.* [Particle Data Group], "Review of Particle Physics," J. Phys. G. **33**, 1 (2006).

[55] J. F. Beacom, N. F. Bell, "Do solar neutrinos decay?," Phys. Rev. D **65**, 113009 (2002) [arXiv:hep–ph/0204111].

[56] H. E. Haber and G. L. Kane, "The search for supersymmetry: probing physics beyond the standard model," Phys. Rep. **117**, 75 (1985).

[57] J. L. Feng, A. Rajaraman and F. Takayama, "Superweakly–interacting massive particles," Phys. Rev. Lett. **91**, 011302 (2003) [arXiv:hep–ph/0302215].

[58] S. A. Bonometto, F. Gabbiani and A. Masiero, "Mixed Dark Matter from Axino Distribution," Phys. Rev. D **49**, 3918 (1994) [arXiv:astro–ph/9305010].

[59] T. Goto and M. Yamaguchi, "Is axino dark matter possible in supergravity?," Phys. Lett. B **276**, 103 (1992).

[60] S. Dodelson and L. M. Widrow, "Sterile Neutrinos as Dark Matter," Phys. Rev. Lett. **72**, 17 (1994) [arXiv:hep–ph/9303287].

[61] X. D. Shi and G. M. Fuller, "A New Dark Matter Candidate: Non–thermal Sterile Neutrinos," Phys. Rev. Lett. **82**, 2832 (1999) [arXiv:astro–ph/9810076].

[62] A. Drukier and L. Stodolsky, "Principles and applications of a neutral–current detector for neutrino physics and astronomy," Phys. Rev. D **30**, 2295 (1984).

[63] M. W. .Goodman and E. Witten, "Detectability of certain dark–matter candidates," Phys. Rev. D **31**, 3059 (1985).

[64] I. Wasserman, "Possibility of detecting heavy neutral fermions in the Galaxy," Phys. Rev. D. **33**, 2071 (1986).

[65] M. C. P. Isaac, "Detection of Dark Matter," AIP Conference Proceedings – December 12, **549**, 177 (2000).

[66] R. Bernabei *et al.*, "DAMA results," [arXiv:arXiv:astro–ph/0305542].

[67] A. Benoit *et al.*, "Improved exclusion limits from the EDELWEISS WIMP search," Phys. Lett. B **545**, 43 (2002) [arXiv:astro–ph/0206271].

[68] D. S. Akerib *et al.* [CDMS Collaboration], "New results from the Cryogenic Dark Matter Search experiment," Phys. Rev. D **68**, 082002 (2003) [arXiv:hep–ex/0306001].

[69] T. C. Weeks, *et al.*, "Observation of TeV gamma rays from the Crab Nebula using the atmospheric Cerenkov imaging technique," Astrophys. J.**342**, 379 (1998).

[70] http://hegra1.mppmu.mpg.de/MAGICWeb/.

[71] http://www.mpi-hd.mpg.de/hfm/HESS/HESS.html/.

[72] D. Hooper and B. Dingus, "Improving the angular resolution of EGRET and new limits on supersymmetric dark matter near the galactic center," arXiv:astro–ph/0212509.

[73] H. A. Mayer–Haesselwander, *et al.,* "High–energy gamma–ray emission from the Galactic Center," Astron. Astrophys **335**, 161 (1998).

[74] V. A. Balkanov *et al.* [BAIKAL Collaboration], "The Lake Baikal neutrino experiment," Nucl. Phys. Proc. Suppl. **87**, 405 (2000) [arXiv:astro–ph/0001145].

[75] E. Andres *et al.*, "The AMANDA neutrino telescope: Principle of operation and first results," Astropart. Phys. **13**, 1 (2000) [arXiv:astro–ph/9906203].

[76] E. Andreas *et al.*, "Neutrino astronomy on ice," Nature **410**, 441 (2001).

[77] E. Aslanides *et al.* [ANTARES Collaboration], "A deep sea telescope for high energy neutrinos," [arXiv:astro–ph/9907432].

[78] J. Ahrens *et al.* [IceCube Collaboration], "Sensitivity of the IceCube detector to astrophysical sources of high energy muon neutrinos," Astropart. Phys. **20**, 507 (2004) [arXiv:astro–ph/0305196].

[79] J. Ahrens *et al.* [The IceCube Collaboration], "IceCube: The next generation neutrino telescope at the South Pole," Nucl. Phys. Proc. Suppl. **118**, 388 (2003) [arXiv:astro–ph/0209556].

[80] S. W. Barwick *et al.* [HEAT collaboration], "Measurements of the cosmic–ray positron fraction from 1–GeV to 50–GeV," Astrophys. J. **482**, L191 (1997) [arXiv:astro–ph/9703192].

[81] S. Coutu *et al.*, "Positron measurements with the heat–pbar instrument," *Proceedings of the 27th International Cosmic Ray Conference (ICRC 2001), Hamburg, Germany, 7–15 Aug 2001.*

[82] S. Coutu *et al.* [HEAT collaboration], "Cosmic–ray positrons: Are there primary sources?," Astropart. Phys. **11**, 429 (1999) [arXiv:astro–ph/9902162].

[83] S. Orito *et al.* [BESS Collaboration], "Precision measurement of cosmic–ray antiproton spectrum," Phys. Rev. Lett. **84**, 1078 (2000) [arXiv:astro–ph/9906426].

[84] T. Maeno *et al.* [BESS Collaboration], "Successive measurements of cosmic–ray antiproton spectrum in a positive phase of the solar cycle," Astropart. Phys. **16**, 121 (2001) [arXiv:astro–ph/0010381].

[85] M. Boezio *et al.* [WiZard/CAPRICE Collaboration], "The cosmic–ray anti–proton flux between 3–GeV and 49–GeV," Astrophys. J. **561**, 787 (2001) [arXiv:astro–ph/0103513].

[86] P. Picozza and A. Morselli, "Antimatter research in space," J. Phys. G **29**, 903 (2003) [arXiv:astro–ph/0211286].

[87] K. A. Olive and D. Thomas, "Generalized Limits to the Number of Light Particle Degrees of Freedom from Big Bang Nucleosynthesis," Astropart. Phys. **11**, 403 (1999) [arXiv:hep–ph/9811444]; E. Lisi, S. Sarkar and F. L. Villante, "Big bang nucleosynthesis limit on N_ν," Phys. Rev. D **59**, 123520 (1999) [arXiv:hep–ph/9901404]; R. H. Cyburt, B. D. Fields, K. A. Olive and E. Skillman, "New BBN limits on Physics Beyond the Standard Model from He4," Astropart. Phys. **23**, 313 (2005) [arXiv:astro–ph/0408033].

[88] M. Drees, Y. G. Kim, M. M. Nojiri, D. Toya, K. Hasuko and T. Kobayashi, "Scrutinizing LSP Dark Matter at the LHC," Phys. Rev. D **63**, 035008 (2001) [arXiv:hep–ph/0007202]; B. C. Allanach, G. Bélanger, F. Boudjema and A. Pukhov, "Require-

ments on collider data to match the precision of WMAP on supersymmetric dark matter," JHEP **0412**, 020 (2004) [arXiv:hep–ph/0410091]; M. M. Nojiri, G. Polesello and D. R. Tovey, "Constraining Dark Matter in the MSSM at the LHC," JHEP, **0603**, 063 (2006) [arXiv:hep–ph/0512204]; E. A. Baltz, M. Battaglia, M. E. Peskin and T. Wizansky, "Determination of Dark Matter Properties at High–Energy Colliders," Phys. Rev. D **74**, 103521 (2006) [arXiv:hep–ph/0602187].